Voltage-dependent Dynamic FRET Signals from the Transverse Tubules in Mammalian Skeletal Muscle Fibers

Marino DiFranco, Joana Capote, Marbella Quiñonez, and Julio L. Vergara

Department of Physiology, David Geffen School of Medicine, University of California Los Angeles, Los Angeles, CA 90095

Two hybrid voltage-sensing systems based on fluorescence resonance energy transfer (FRET) were used to record membrane potential changes in the transverse tubular system (TTS) and surface membranes of adult mice skeletal muscle fibers. Farnesylated EGFP or ECFP (EGFP-F and ECFP-F) were used as immobile FRET donors, and either non-fluorescent (dipicrylamine [DPA]) or fluorescent (oxonol dye $DiBAC_4(5)$) lipophilic anions were used as mobile energy acceptors. Flexor digitorum brevis (FDB) muscles were transfected by in vivo electroporation with pEGFP-F and pECFP-F. Farnesylated fluorescent proteins were efficiently expressed in the TTS and surface membranes. Voltage-dependent optical signals resulting from resonance energy transfer from fluorescent proteins to DPA were named QRET transients, to distinguish them from FRET transients recorded using $DiBAC_4(5)$. The peak $\Delta F/F$ of QRET transients elicited by action potential stimulation is twice larger in fibers expressing ECFP-F as those with EGFP-F (7.1% vs. 3.6%). These data provide a unique experimental demonstration of the importance of the spectral overlap in FRET. The voltage sensitivity of QRET and FRET signals was demonstrated to correspond to the voltage-dependent translocation of the charged acceptors, which manifest as nonlinear components in current records. For DPA, both electrical and QRET data were predicted by radial cable model simulations in which the maximal time constant of charge translocation was 0.6 ms. FRET signals recorded in response to action potentials in fibers stained with $DiBAC_4(5)$ exhibit $\Delta F/F$ amplitudes as large as 28%, but their rising phase was slower than those of QRET signals. Model simulations require a time constant for charge translocation of 1.6 ms in order to predict current and FRET data. Our results provide the basis for the potential use of lipophilic ions as tools to test for fast voltage-dependent conformational changes of membrane proteins in the TTS.

The Journal of General Physiology

INTRODUCTION

Nonradiative energy transfer (Föster energy transfer) is a valuable tool to measure intra- and intermolecular distances (within the 1–10-nm range) between donor and acceptor fluorophores (FRET pairs) (Stryer and Haugland, 1967; Clegg, 1995). The steep dependence of FRET on the distance between interacting fluorophores, and the fact that the thickness of biological membranes is within the effective range of FRET interaction for commonly used fluorophores, have been exploited in the design of photometric methods to measure transmembrane potential. Thus, FRET pairs between acceptor (donor) lipophilic mobile ions and donor (acceptor) fluorophores bound (or anchored) at either side of membrane have been reported (Gonzalez and Tsien, 1995, 1997). The voltage dependence of the FRET signals stems from the voltage-dependent translocation of a lipophilic ion between positions close to the inner and outer leaflet of the membrane, representing two energy minima (Gonzalez and Tsien, 1995, 1997; Chanda et al., 2005). Both the mobile and fixed components of voltage-sensing FRET pairs were initially envisaged as synthetic chemical compounds staining either side of the cell membrane (Gonzalez and Tsien, 1995, 1997). However, a recently described hybrid voltage-sensing system relies on the FRET interaction between recombinant farnesylated EGFP (EGFP-F) expressed at the surface membrane of neurons and cells in culture and the nonfluorescent absorber dipicrylamine (DPA) (Chanda et al., 2005). This method takes advantage of well-studied targeting mechanisms (through farnesylation signals) by which c-Ha-Ras proteins are anchored to the inner leaflet of the cell membrane (Aronheim et al., 1994; Moriyoshi et al., 1996; Zhang and Casey, 1996). A voltage-dependent optical signal is then generated by the resonance interaction between excited EGFP-F molecules anchored to the membrane, which act as donors, and DPA molecules that work as nonfluorescent mobile acceptors. In this case, the mechanism of energy transfer is the same as in FRET (hence the primary theoretical formulas can be used [Clegg, 1995; Siegel et al., 2000; Selvin, 2002]), but since the only detectable optical change is the quenching of the donor fluorescence by the acceptor, it is called QRET signal. We will adopt this

Correspondence to Julio L. Vergara: jvergara@mednet.ucla.edu

Abbreviations used in this paper: AP, action potential; $DiBAC_4(5)$, bis-(1,3-dibutylbarbituric acid)pentamethine oxonol; DPA, dipicrylamine; EGFP-F or ECFP-F, farnesylated EGFP or ECFP; FDB, flexor digitorum brevis; FRET, fluorescence resonance energy transfer; HP, holding potential; IOS, interossei; TPLSM, two-photon laser scanning microscopy; TTS, transverse tubular system.

nomenclature to distinguish this type of signal from those generated by two fluorophores in which FRET optical changes, "donor quenching" and "acceptor-sensitized emission," can be detected (Gonzalez and Tsien, 1995).

The hybrid QRET pair has some advantages over methods based on the use of synthetic fluorophores because the expression of the donor can be made cell type dependent, thus allowing for the recording of electrical activity from specific subpopulation of cells. Furthermore, the small size and small translocation time constant of DPA make the EGFP-F//DPA QRET pair capable of tracking rapid changes in membrane potential (frequency response >2 kHz) (Fernandez et al., 1983).

In the current report, we demonstrate that murine skeletal muscle fibers readily express EGFP-F, and the novel farnesylated cyan fluorescent protein (ECFP-F), in the surface and transverse tubular system (TTS) membranes. Further, we show that these anchored fluorescent proteins can be combined with DPA to dynamically probe changes in membrane potential arising at this prominent muscle membrane compartment. We also report a novel hybrid FRET system to follow changes in membrane potential based on the use of EGFP-F as a stationary donor and the dye bis-(1,3-dibutylbarbituric acid)pentamethine oxonol ($DiBAC_4(5)$) as a mobile acceptor. Finally, the voltage-sensing characteristics of FRET-based systems were analyzed in the light of the predictions from a radial cable model of the muscle fiber (Ashcroft et al., 1985; Kim and Vergara, 1998b) in which a two-state model (Fernandez et al., 1983) of the voltage-dependent translocation of mobile ions was incorporated in the surface and TTS membranes.

MATERIALS AND METHODS

Biological Preparation

Animal handling and protocols were performed according to the guidelines laid down by the UCLA Animal Research Committee. Single fibers from flexor digitorum brevis (FDB) and interossei (IOS) muscles from the lower limb of 2–6-mo C57BL/10J mice were used. Intact fibers were obtained by enzymatic dissociation and transferred to an optical chamber, which was mounted on the stage of an inverted microscope (IX-71, Olympus) equipped with an epifluorescence attachment (DiFranco et al., 2005; Woods et al., 2005).

Plasmids for Recombinant Farnesylable and Soluble EGFP and ECFP

The pEGFP-F vector, encoding for recombinant EGFP containing a 20–amino acid farnesylation signal from the c-Ha-Ras protein, was commercially available (CLONTECH Laboratories, Inc.). It was amplified and used for in vivo electroporation without further modification. A novel plasmid encoding for the same farnesylation signal, but attached to ECFP (ECFP-F) was constructed by us by replacing the NheI-BsrGI fragment of pEGFP-F with the NheI-BsrGI fragment from pECFP-C1 (CLONTECH Laboratories, Inc.). Plasmids encoding for EGFP and ECFP N-tagged with a 6-His sequence (pEGFPN1-histag and pECFPN1-histag, respectively) were engineered from pECFP-N1 and pEGFP-N1 (CLONTECH Laboratories, Inc.).

Transfection and Expression of pECFP-F and pEGFP-F in Muscle

FDB and IOS muscles were transfected in vivo using an electroporation protocol similar to that reported elsewhere (DiFranco et al., 2006). In brief, as illustrated in Fig. 1, 5 μl of 2 mg/ml hyaluronidase (type IV-S from bovine testes, Sigma-Aldrich) dissolved in medical grade sterile saline was injected subcutaneously in the lower limb footpads using 33-gauge needles (Hamilton). 1 h later, 25 μg pDNA (5 μg/μl in sterile buffer TE) was injected the same way. After 10 min, the muscles were electroporated by applying 20 pulses (1Hz, 20 ms duration each) between two subcutaneous electrodes (see Fig. 1). The amplitude of the pulses was adjusted to apply a field of 100 V/cm. The electrodes consisted of disposable sterile gold-plated acupuncture needles 0.2 × 25 mm (Lhasa OMS, Inc.) which were connected via microclips to a medical grade stimulator (Grass S88, Grass-Telefactor). Injections and electroporation were performed under anesthesia (3% isoflurane in O_2, 2 liters/min). Transfected muscles were used for fiber isolation 2–10 d after electroporation. The efficiency of expression and intracellular targeting of EGFP-F and ECFP-F in the muscle fibers were verified in two-photon laser scanning microscopy (TPLSM) images acquired with a 20×, 0.95 NA (Olympus XLUMPLANFL) water immersion objective. The TPLSM system was based on an upright microscope (BX51WI, Olympus) equipped with a tunable wavelength Chameleon Ti/Sapphire laser (Coherent) and a Radiance 2000 Scanning Head (Bio-Rad Laboratories). Both ECFP-F and EGFP-F were excited at 890 nm and the fluorescence detected through 450//460-500 and 500//510-560 dichroic//band-pass filter combinations, respectively. The precise targeting of farnesylated fluorescent proteins was determined in muscles transfected with pECFP-F and subsequently stained with di-8-ANEPPS using TPLSM. Both ECFP-F and di-8-ANEPPS were excited at 890 nm and their emission was separated with a 550-nm dichroic mirror, and filtered with 460–500 and 580–630-nm band-pass filters, respectively. Two photon images were analyzed using commercial (LaserSharp 2000MP, Bio-Rad Laboratories, Carl Zeiss MicroImaging, Inc.) and/or public domain image analysis software packages (ImageJ). The images were finally rendered in 256 pseudocolor intensity levels using monochromatic pseudocolor scales that match the color of the respective fluorophores' emission.

EGFP and ECFP Isolation from Muscle Tissue

For mass production, extraction, and purification of EGFP and ECFP, mice lower limb muscles were used according to the protocols described elsewhere (DiFranco et al., 2006). In this work the leg muscles from 10 mice were transfected with either pEGFP-histag or pECFP-histag, which resulted in sufficient quantities of 6-His–tagged EGFP and ECFP to allow for their purification to homogeneity (∼98%) by gel filtration (Analytical Superdex 200, Amersham Biosciences) followed by elution through cobalt Talon columns (CLONTECH Laboratories Inc.), ultimately yielding ∼1.5 mg of each protein. Direct sequencing of both plasmid constructs was performed in order to verify their fidelity with respect to the original sequences (Prasher et al., 1992; Heim and Tsien, 1996; Rizzo et al., 2004); this was particularly relevant in the case of pECFP-histag since the fluorescence- enhancing mutation H148D (Rizzo et al., 2004) was absent in our constructs.

Electrophysiology

A two-microelectrode amplifier (Dagan, TEV-200A) was used for stimulation and recording of electrical signals from isolated muscle fibers under both current (CC) and voltage-clamp (VC) configurations, as described elsewhere (Woods et al., 2004; DiFranco et al., 2005; Woods et al., 2005). To improve the frequency response of the voltage-clamp system, the microelectrodes were drawn to the largest tip compatible with fiber viability. Voltage microelectrodes

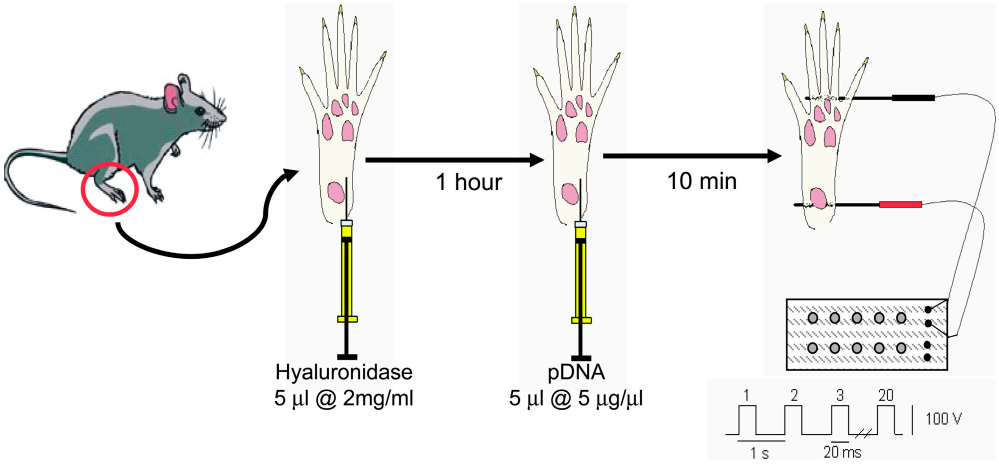

Figure 1. Plasmid DNA transfection in murine foot muscles by in vivo electroporation. The schematic diagram indicates the sites where injection and electrode needles were placed in mice feet with respect to the positions of footpads and toes (plantar view). See text for a detailed explanation of the protocols.

were filled with either 1 M KCl (CC) or 2 M CsCl (VC) and had resistances ~10 MΩ; current electrodes were filled with either K (CC) or Cs (VC) based internal solutions (see Solutions) and had resistances of ~15 MΩ. The tips of the microelectrodes were placed ~10 µm apart along the midline of the muscle fiber. Microelectrode capacitance was maximally compensated with a positive feedback circuit. In CC experiments the muscle fibers were bathed in Tyrode solution and the membrane potential was adjusted to −90 mV by injecting a steady current, typically <15 µA/cm² (Woods et al., 2004); action potentials (APs) were elicited with 0.5-ms current pulses. In VC experiments, the fibers were rendered electrically passive by replacing Tyrode with V-clamp external solution (see Solutions) and maintained at a −90 mV holding potential (HP). A 16-bit data acquisition board (National Instruments, PCI-MIO-16XE-10) under program control (Labview, National Instruments) was used to synchronously generate stimulus pulses and to acquire data. Total membrane capacitance was calculated by integration of current records subtracted from linear leak. Unless otherwise stated, voltage and current records were filtered at 5 kHz with 8-pole Bessel filters (Frequency Devices), and digitized at >30 kHz. Experiments were performed at room temperature (21°C).

Muscle Fiber Staining with Potentiometric Dyes and DPA

Staining of the muscle fibers with DPA (ammonium salt, City of Chemicals) and $DiBAC_4(5)$ (Invitrogen) was performed in the recording chamber by transient perfusion (5–10 min) with dye-containing external solutions (5 µM) followed by extensive wash with dye-free solution. Solutions were made fresh by dilution from DMSO stocks (10–100 mM). Staining with di-8-ANEPPS was as previously described (DiFranco et al., 2005).

Optical Recordings

The optical arrangement for recording global fluorescence, QRET, and FRET signals is similar to that described elsewhere (DiFranco et al., 2005). Light from a Tungsten halogen lamp, filtered using the filter configurations described in Table I, was focused onto the fibers' medial plane to form an ~15-µm diameter disc using a 100×, 1.4 NA oil immersion objective (Olympus). The fluorescence image of the disc was focused on a PIN photodiode (UV100, United Detector Technologies) connected to a current-to-voltage converter (Kim and Vergara, 1998a; Woods et al., 2004; DiFranco et al., 2005). Low pass–filtered (2–5 kHz) single sweep optical signals were acquired in synchrony with electrical signals (membrane voltage and current) and normalized to the prestimulus baseline (ΔF/F). Movement artifacts in the optical signals were prevented by the use of 50 mM EGTA in the internal solutions (see below).

Spectral Properties of Dyes and Fluorescent Proteins

The absorbance spectra of DPA and $DiBAC_4(5)$ dissolved in water and methanol, and of the fluorescent proteins in internal solution, were measured in an HP 8453 spectrophotometer. The fluorescence spectra of $DiBAC_4(5)$, EGFP, and ECFP in solution were measured in a FluoroMax-3 Spectrofluorimeter (Horiba Jobin Yvon). The fluorescence spectra of EGFP-F and ECFP-F were measured in vivo from isolated fibers mounted in the fluorescence microscope described above but additionally equipped with a fiber optic–coupled spectrofluorimeter (EPP2000, StellarNet). The custom-made cube configuration for the acquisition of fluorescence spectra in vivo was 400–445//450//470-650.

The quantum yield (Φ) of EGFP and ECFP was determined using fluorescein as a standard reference of known Φ following protocols described elsewhere (Williams et al., 1983; Magde et al., 2002); solutions of EGFP (ECFP) at four concentrations were prepared such that their absorbance values, measured at 460 (434) nm, ranged between 0.005 and 0.1. Fluorescein solutions in 100 mM NaOH with the same absorbance values were also prepared. Then, the fluorescence emission spectra of the proteins and fluorescein solutions (excited at the wavelengths above) were recorded. These fluorescence spectra were integrated (Berkeley Madonna, Oster & Macer) and the values of the integrals were plotted as a function of the corresponding absorbance for each solution. These data were fitted to straight lines and the slopes (m) were used to calculate the quantum yield according to the formula (Williams et al., 1983): $\Phi_x = \Phi_{Fl} \bullet (m_x/m_{Fl}) \bullet (n^2_x/n^2_{Fl})$, where x= EGFP or ECFP, and n is the refractive index of the solutions, which were measured (N = 3) using an Abbe-type refractometer (Bausch and Lomb). The values of n for NaOH and internal solutions were 1.336 ± 0.0006 and 1.342 ± 0.0007, respectively. The value of Φ_{Fl} in 0.1 NaOH was assumed to be 0.92, as suggested from the literature consensus (Williams et al., 1983). For both proteins, measurements were made in two batches of four concentrations each, yielding values of 0.6 ± 0.12 and 0.62 ± 0.09 for EGFP and ECFP, respectively.

Data Analysis

Optical signals were analyzed and processed using a custom program written in Delphi (Borland Corporation) and Origin 7.5 (OriginLab). Kinetic parameters and amplitudes of optical signals were determined as described previously (DiFranco et al., 2002; Woods et al., 2004).

Current records obtained from voltage-clamped fibers under passive conditions were integrated using a custom written LabView (National Instruments) program and analyzed for best-fit parameters using least square fitting routines in Berkeley Madonna (Oster & Macey) and Origin 7.5. The on and off decay kinetics

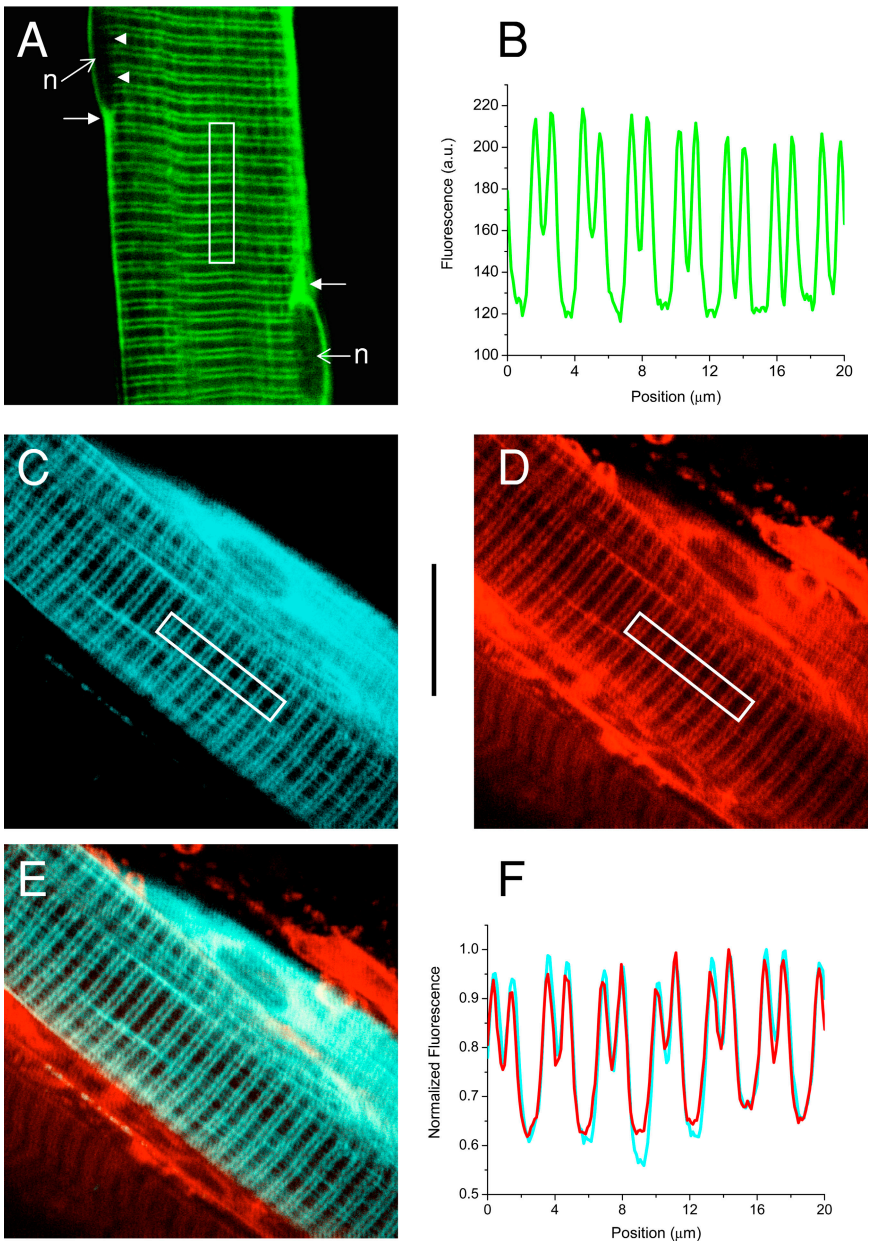

Figure 2. Membrane expression of EGFP-F and ECFP-F in FDB muscle fibers. (A) TPLSM image section obtained at the medial plane of a muscle fiber expressing EGFP-F. n denotes nucleus; arrowheads point to the cytoplasmic side of a nucleus; arrows point toward areas of increased fluorescence close to the poles of nuclei. (B) Fluorescence intensity profile obtained from the area delimited by the white rectangle in A. (C and D) TPLSM image sections of an FDB muscle transfected with pECFP-F and stained extracellularly with di-8-ANEPPS. ECFP-F and di-8-ANEPPS fluorescence images are shown in C and D, respectively. (E) Superimposition of image sections in C and D. (F) Normalized fluorescence intensity profiles measured from the area delimited by the rectangles in Fig. 2, C (cyan trace) and D (red trace). The vertical calibration bar is 20 μm and applies to all the images.

of the capacitive currents were fitted to the double exponential function

$$I(t) = I_{SS} + I_1 e^{\frac{-t}{\tau_1}} + I_2 e^{\frac{-t}{\tau_2}},$$

and integrated numerically to calculate the charge mobilized. I_{SS} is the steady-state current (leak) during the pulse and I_1 and τ_1 and I_2 and τ_2 are the amplitude and time constant of each transient component, respectively.

Solutions

The compositions of the solutions (in mM) were as follows: Tyrode: 150 NaCl, 2.5 KCl, 2 $CaCl_2$, 1 $MgCl_2$, 10 dextrose, 10 MOPS, 0.5 Trolox, pH adjusted with NaOH; V-clamp external: 182 TEA-OH, 5 CsOH, 3.25 $Ca(OH)_2$, 5 dextrose, 15 MOPS, 0.0002 TTX, 0.002 verapamil, 1.0 9-ACA, 0.5 Trolox, pH adjusted with H_2SO_4; K-internal: 50 aspartic acid, 20 MOPS, 5 ATP-Tris, 5 $MgCl_2$, 50 EGTA, 5 di-Na phosphocreatine, 3 reduced glutathione, 5 dextrose, and 0.1 mg/ml phosphocreatine kinase, pH adjusted with KOH; Cs-internal: same as K-internal, but pH adjusted with CsOH. Osmolarity and pH of all the solutions were set at 300 mOsm and 7.4, respectively.

RESULTS

Targeting of Farnesylated Fluorescent Proteins to External Muscle Membrane Systems

A prerequisite for the use EGFP-F or ECFP-F as effective immobile components of voltage-sensing QRET pairs is to demonstrate that they are specifically anchored at the desired external membrane compartments, which in the case of skeletal muscle are the TTS and sarcolemma

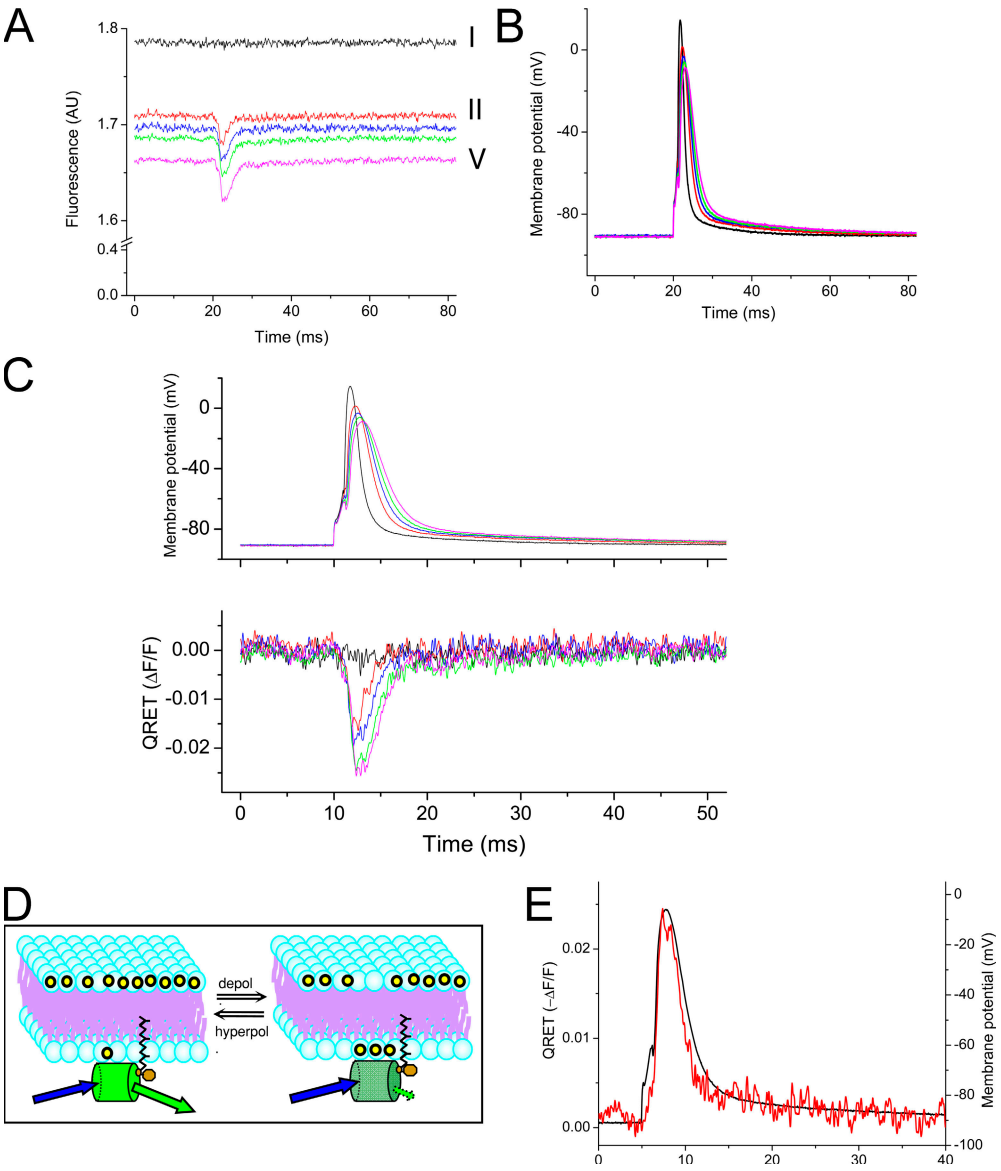

Figure 3. Steady-state and dynamic AP-dependent quenching of EGFP-F fluorescence by DPA. (A) Raw EGFP-F fluorescence before (trace I) and during DPA application (traces II–V). Records were acquired at 0, 1/2, 1, 2, and 3 min after DPA perfusion. Suprathreshold stimuli were delivered at $t = 20$ ms. Note the absence of QRET response in record I and the increasing amplitude of the AP-dependent fluorescence transients as perfusion time progresses. (B) APs that elicited the transients in A (the colors are matched). (C, bottom) $\Delta F/F$ rendition (in an expanded time scale) of the QRET transients in panel A. (top) APs corresponding to QRET transients. (D) Schematic model of the voltage-dependent translocation of DPA and its interaction with EGFP-F. Different colors and length of the arrows were chosen to highlight the wavelength of excitation and emission, and the change in fluorescence intensity of EGFP. (E) Kinetic comparison of the largest QRET signal in A and C with its corresponding AP. The optical signal is shown inverted ($-\Delta F/F$).

membranes, while leaving the internal membrane compartments untagged. We used TPLSM to examine the specificity of the intracellular targeting of these proteins to the membrane systems of FDB and IOS muscle fibers. Fig. 2 A shows a TPLSM section of an FDB fiber obtained 2 d after transfection with pEGFP-F. As can be seen the fluorescence is restricted to the perimeter of the fiber and to bands oriented orthogonally to the long axis of the fiber, while it is mostly absent in the myoplasm and the nucleoplasm. The fluorescent bands are arranged in pairs, displaying a pattern reminiscent of that described previously in mammalian fibers stained with di-8-ANEPPS (DiFranco et al., 2005). It should be noted that EGFP-F is not targeted to the nuclear envelope, as evidenced by the absence of fluorescence in the internal (myoplasmic) face of the nuclei (Fig. 2 A, arrowheads). It is also observed that the poles of this organelle are associated with regions of high fluorescence intensity that extend in the subsarcolemmal region alongside the fiber (Fig. 2 A, arrows).

A more definite proof of the exclusive targeting of farnesylated fluorescent proteins to the TTS membrane and sarcolemma was obtained in fibers expressing ECFP-F and subsequently stained with di-8-ANEPPS. The TPLSM image shown in Fig. 2 C illustrates that the membrane targeting of ECFP-F is identical to that exhibited by EGFP-F. Furthermore, Fig. 2 D shows, for comparison, that the di-8-ANEPPS staining of the TTS membranes displays an identical pattern to that exhibited by farnesylated fluorescent proteins. The superposition of ECFP-F and di-8-ANEPPS images (Fig. 2 E) demonstrates that both fluorophores colocalize at the level of the TTS and surface membranes. This result is further stressed by the line profiles of Fig. 2 F. The cyan and red traces represent normalized intensity profiles obtained from the rectangles in Fig. 2 (C and D), respectively. It can be seen that

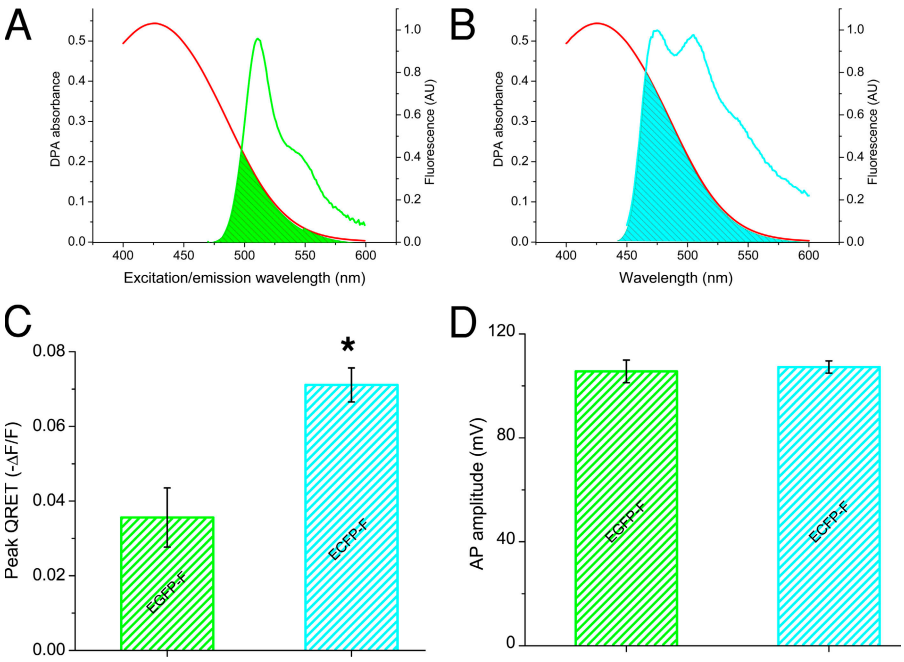

Figure 4. QRET transient amplitude and DPA//EGFP-F and DPA//ECFP-F spectral overlap. (A) Spectral overlap between DPA absorption spectrum (red trace) and EGFP-F normalized emission spectrum (green trace). (B) Spectral overlap between DPA absorption spectrum (red trace) and ECFP-F normalized emission spectra (cyan trace). EGFP-F and ECFP-F emission spectra were determined in vivo and DPA absorption spectrum was measure in vitro. (C) Peak amplitude of EGFP-F (green hatched bar) and ECFP-F (cyan hatched bar) QRET transients evoked by AP stimulation. The averages values (in $-\Delta F/F$) were calculated from 6 and 12 fibers for EGFP-F and ECFP-F, respectively. The error bar is the SEM. The asterisk indicates statistical significance ($P < 0.01$). Signals were acquired using the filter combinations in Table I. (D) Average amplitude of the APs that elicited the QRET transients in C.

both profiles closely superimpose each other, thus demonstrating that ECFP-F is targeted to the TTS and surface membranes. Possible cross bleeding of the emission of both fluorophores was discarded by imaging fibers either expressing ECFP-F or stained with di-8-ANEPPS under the same conditions above (unpublished data).

Action Potential–dependent QRET between EGFP-F and DPA

The fluorescence observed at the surface and TTS membranes in images of muscle fibers expressing EGFP-F can be detected as a steady level of intensity in quiescent fibers mounted for electrophysiological experiments in the fluorescence microscope. As shown in trace I of Fig. 3 A, this baseline fluorescence is insensitive to changes in membrane potential when the fiber is stimulated to elicit an AP (largest record in Fig. 3 B). The rest of the traces in Fig. 3 A illustrate the consequences that external perfusion with Tyrode containing 5 μM DPA has on the optical signals recorded from EGFP-F–transfected fibers. First, there is a progressive decrease in the baseline fluorescence reaching a steady state at ∼90% of the one previous to DPA exposure in ∼3 min (trace V); this decrement in fluorescence could be partially explained by the absorbance of excitation light by DPA staining the muscle membranes. In addition, it could reflect the steady-state QRET interaction between DPA and EGFP-F at the membranes. This latter possibility is reinforced by the detection of rapid negative changes in fluorescence (QRET transients; Fig. 3 A, traces II–V), which are elicited in response to AP stimulation (Fig. 3 B). QRET transients become progressively larger as the staining of the fiber membranes with DPA progresses in time. However, their amplitude reaches a maximum within ∼3 min (Fig. 3 A, trace V) after the initiation of the exposure to DPA. Both the magnitude of the basal fluorescence reduction and the maximal amplitude of the QRET signals were found to depend on the DPA concentration (unpublished data); furthermore, they were not reverted by DPA washout. The progressive increase in magnitude of the QRET signals after exposure of the fiber to DPA is better illustrated when these optical signals are expressed in ΔF/F units and superimposed for comparison (Fig. 3 C, bottom). It can be observed that the peak ΔF/F of the QRET signals increased from ∼1% when recorded 30 s after switching to DPA-containing solution, to ∼3% at the steady state. It should be noted that exposure to DPA is also accompanied with changes in the electrical properties of the muscle fiber. As illustrated in the top panel of Fig. 3 C, DPA induces an increase in the threshold for AP stimulation, a reduction in the amplitude of the AP, and a noticeable increase in AP duration. As will be shown later, these changes are expected and could be explained on the basis of the additional membrane capacitance contributed by DPA (Fernandez et al., 1983; Oberhauser and Fernandez, 1995). Keeping these considerations in mind, a simple explanation for the results reported in Fig. 3 (A and C) is presented in the scheme of Fig. 3 D. Due to its lipophilic properties and negative charge, DPA (yellow circles) partitions in a voltage-dependent manner across the surface and TTS membranes of the muscle fiber as it occurs in lipid bilayers and other excitable cells (Benz et al., 1976; Benz and Nonner, 1981; Fernandez et al., 1983). At negative potentials (i.e., the −90 mV resting membrane potential of the muscle fibers) the equilibrium distribution of dye molecules across the membrane favors their partitioning at the external leaflet, while

TABLE I

Cube Configuration for Dynamic Recording of Voltage-dependent Optical Signals

Indicator	Type of signal	Cube name	Excitation	Dichroic	Emission
			nm	*nm*	*nm*
EGFP-F//DPA	QRET	EGFP-QRET	460–500	500	513–558
ECFP-F//DPA	QRET	ECFP-QRET	420–450	450	460–500
EGFP-F//DiBAC$_4$(5)	Donor FRET	Donor-EGFP	460–500	500	513–558
	Acceptor FRET	Sensitized-DiBAC	460–500	550	590LP

membrane depolarizations increase the probability of their translocation toward the internal leaflet (Benz and Nonner, 1981). Furthermore, since DPA's absorption spectrum overlaps with the emission spectrum of EGFP-F (see Fig. 4), its translocation from the outer to the inner leaflet of surface and TTS membranes in response to the depolarization of the muscle fiber during the AP leads to an increased quenching of the EGFP-F fluorescence due to an increased QRET interaction between both molecules (Chanda et al., 2005). A corollary of this model, as suggested above and expanded later in the paper, is that there should be QRET between DPA and EGFP-F at the −90 mV resting potential of the muscle fibers since at this potential the probability of DPA being in the internal leaflet of the membranes is nonzero.

An important feature of the QRET signals shown in Figs. 3 is that they may arise mostly from contributions at the TTS membranes since this is the membrane compartment that contributes with the majority of the EGFP-F fluorescence (see Fig. 2, A and C). To further explore this possibility, the largest QRET signal from the bottom panel in Fig. 3 C was inverted and plotted superimposed with the corresponding electrical record of the AP in Fig. 3 E. It can be seen that both the rising and falling phases of the QRET transient differ slightly from the corresponding phases of the AP. Namely, the initial response to the stimulus pulse, which is prominently observed in the electrical record of the AP, is less noticeable in the QRET signal. Likewise, the repolarization phase of the AP decays toward its resting value at a slower rate than that of the QRET signal. This peculiar mismatching between the kinetics of QRET signals and APs is reminiscent of results obtained from mammalian muscle fibers stained with di-8-ANEPPS (DiFranco et al., 2005). As reported, signals obtained with this electrochromic potentiometric indicator capable of linearly tracking rapid changes in membrane potential (Bedlack et al., 1992; Rohr and Salzberg, 1994; Kim and Vergara, 1998b; DiFranco et al., 2005) depict the overall electrical response of the TTS, which in mammalian fibers seems to be shortened by the existence of a prominent K conductance (DiFranco et al., 2005). In this context, it is interesting to note that the results shown in Fig. 3 E may suggest that the rate of translocation of DPA in the TTS membranes is fast enough to confer the EGFP-F//DPA pair a frequency response suitable to faithfully track the AP waveform in this membrane compartment. A more direct analysis of this possibility will be provided later in this paper.

Spectral Overlap and QRET Signals

From FRET theoretical principles, a donor fluorophore, after being excited, transfers energy to an acceptor in a distance-dependent fashion according to the well-known formula (Stryer and Haugland, 1967; Clegg, 1995):

$$E = \frac{1}{1+\left(\frac{R}{R_0}\right)^6}, \tag{1}$$

where E is the efficiency of energy transfer, R is the distance between the interacting molecules, and R_o is a constant whose value depends on their relative orientation and spectral properties. More precisely,

$$R_0 = 0.021\sqrt[6]{J\Phi_D n^{-4}\omega^2}, \text{ (nm)} \tag{2}$$

where J represents the spectral overlap of the donor emission with the acceptor absorbance, Φ_D is the quantum yield of the donor, n is the refractive index of the medium, assumed to be 1.29 for membrane-bound probes (Selvin, 2002), and ω is a geometric factor accounting for the relative orientation of the transition dipoles of the donor and acceptor, which will be arbitrarily approximated to be 2/3 (Patterson et al., 2000; Selvin, 2002). The value of J was calculated using the formula (Selvin, 2002):

$$J = \frac{\int \varepsilon_{DPA}(\lambda) f_D(\lambda)\lambda^4 d\lambda}{\int f_D(\lambda) d\lambda}, \quad (\mathrm{M^{-1}cm^{-1}nm^4}) \tag{3}$$

where $\varepsilon_{DPA}(\lambda)$ represents the molar absorption spectrum of DPA, calculated as the normalized absorption spectrum multiplied by the maximum molar extinction coefficient (20,000 $M^{-1}cm^{-1}$ in water), $f_D(\lambda)$ is the peak-normalized fluorescence emission spectrum of the donor, and λ is the wavelength. Fig. 4 A shows the spectral properties of the EGFP-F fluorescence superimposed with the normalized absorption spectrum of DPA, highlighting their relatively poor spectral overlap (hatched area). From these curves, a value of $2.8 \times 10^{14}\ M^{-1}cm^{-1}nm^4$ was calculated for $J^{EGFP//DPA}$. By replacing this value in Eq. 2, and using the average

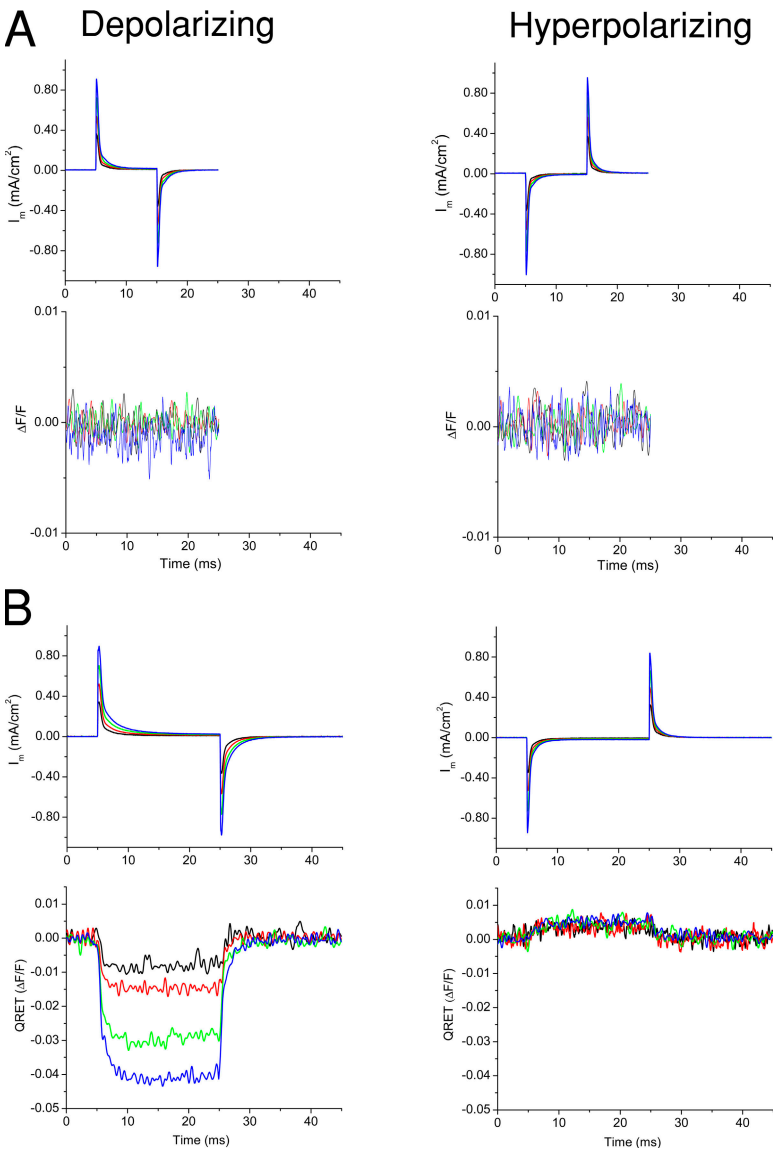

Figure 5. Effects of DPA on the electrical and optical properties of a voltage-clamped skeletal muscle fiber expressing EGFP-F. The fiber was clamped at an HP = −90 mV and stimulated with depolarizing and hyperpolarizing voltage pulses of 40, 60, 80, and 100 mV. Data in A and B were obtained before and after DPA staining, respectively. (A) Top panels show capacitive currents in response to 10-ms depolarizing (left) or hyperpolarizing (right) pulses. Bottom panel shows, in an expanded ordinate scale, the corresponding ECFP-F fluorescence records. (B) Capacitive (top) currents and QRET transients (bottom) in response to 20-ms depolarizing (left) and hyperpolarizing (right) voltage-clamp pulses from the same fiber in A, after DPA staining. The rising phase of QRET transients elicited by depolarizing pulses could be adjusted to single exponential functions with τ = 0.4, 1.1, 1.1, and 1.2 ms for the black, red, green, and blue traces, respectively.

measured value of Φ_D = 0.6 for EGFP (Patterson et al., 2001), we calculate that $R_0^{EGFP//DPA}$ = 3.63 nm for the EGFP-F//DPA pair, a value similar to the 3.7 nm reported previously (Chanda et al., 2005). Similar calculations, but using the absorption spectrum of DPA in methanol, which is slightly blue shifted with respect to that in water (unpublished data), yielded a ∼3% smaller value of $R_0^{EGFP//DPA}$. From Eqs. 2 and 3, it can be predicted that increasing the spectral overlap between donor and acceptor should result in a larger R_0 and thus to a more efficient energy transfer, potentially leading to larger QRET signals. Consequently, we decided to investigate whether ECFP-F significantly enhances the FRET interaction with DPA and, to this end, engineered a plasmid coding for this protein. As shown in Fig. 2 C, ECFP-F was identically expressed in the TTS membrane of muscle fibers as compared with EGFP-F. Fig. 4 B shows that in fact the in vivo spectrum of ECFP-F has a significantly broader overlap with DPA than EGFP-F (Fig. 4 A). The value of R_0 calculated from these data (ECFP-F//DPA pair), using the average measured value of Φ_D = 0.62 for ECFP, was $R_0^{ECFP//DPA}$ = 4.2 nm. This calculation resulted in ∼3% smaller values of $R_0^{ECFP//DPA}$ when the methanol absorption spectrum of DPA was used. Interestingly, and in agreement with the expectations, pooled data show that on average the amplitude of AP-evoked QRET signals recorded from ECFP-F–transfected muscle fibers in the presence of DPA are significantly larger (approximately twofold) than those recorded at identical conditions from fibers expressing EGFP-F (Fig. 4 C). Panel D demonstrates that differences in QRET signals were not due to AP differences. Also, the difference in amplitude between ECFP-F//DPA and EGFP-F//DPA QRET transients were not dependent on the filter combination used to detect them since ΔF/F values almost identical to those reported in Fig. 4 (within ∼3% error)

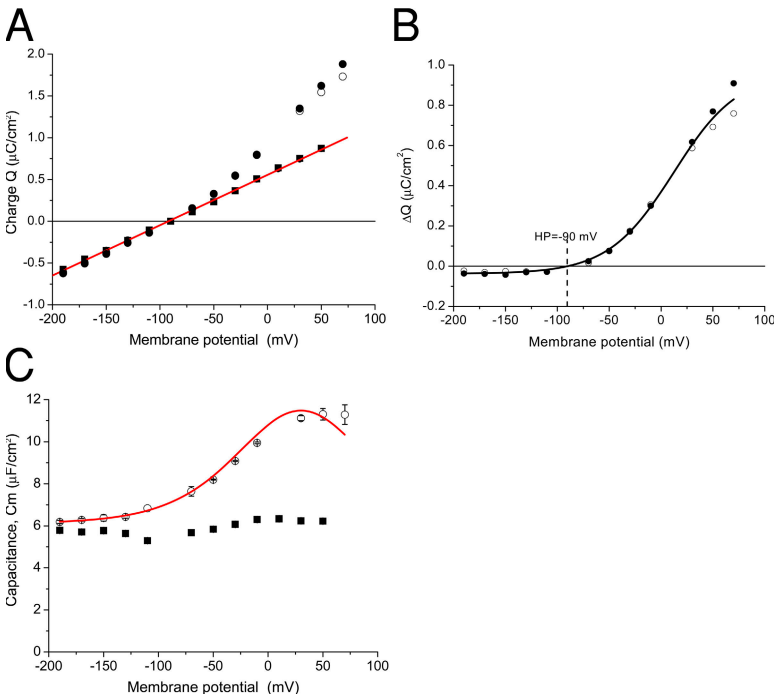

Figure 6. Voltage dependence of DPA effects on steady-state electrical properties of muscle fibers. (A) Total charge mobilized in response to voltage pulses in a fiber expressing ECFP-F, measured before (control, squares) and after DPA staining (circles). The charge was calculated by integration at the on (open symbols) and off (filled symbols) of capacitive currents, normalized by the fiber surface area. The charge under control conditions was fitted to a linear regression (solid line, r = 0.9). (B) The difference between charge after DPA staining and the linear regression gives the extra charge contributed by DPA (on and off are open and filled circles, respectively). Data were fitted to a Boltzmann distribution using Eq. 4 (solid line). (C) Membrane capacitance before (filled squares) and after (open circles) DPA staining. The membrane capacitance at each membrane potential was calculated by dividing the charge (average of on and off) by the magnitude of the pulse. The capacitance after DPA staining was fitted to Eq. 5 (solid line).

were obtained in control experiments (not depicted) using six alternative filters sets with different emission bandwidths than those in Table I.

The above results not only show that ECFP-F//DPA may be a superior voltage-dependent FRET pair than EGFP-F//DPA (thus providing less noisy signals), but also that the comparison between both FRET pairs may serve as an experimental test for the validity of FRET theoretical predictions. For example, using a first order approximant for a random distribution of donor and acceptor molecules in the membrane plane, which is valid for donor–acceptor distances $R \geq 1.7R_0$ (Shaklai et al., 1977; Dewey and Hammes, 1980), the ratio between the efficiency of the ECFP-F//DPA pair, with respect to that of the EGFP-F//DPA pair, should be

$$\left(\frac{R_0^{ECFP//DPA}}{R_0^{EGFP//DPA}}\right)^6 \sim 2.4.$$

Interestingly, this value is larger than the nearly twofold ratio experimentally measured between ΔF/F values for these QRET pairs (as shown in Fig. 4), suggesting that the average effective distance between acceptors and donors in the membrane are shorter than $1.7 \times R_0^{ECFP//DPA} \sim 7.1$ nm.

Voltage Dependence QRET between ECFP-F (EGFP-F) and DPA

The voltage dependence of QRET between ECFP-F and DPA was further studied under voltage-clamp conditions in fibers rendered passive by perfusion with V-clamp solution (see Materials and methods). Step voltage pulses were applied to fibers expressing ECFP-F or EGFP-F and stained with DPA; the evoked QRET transients were recorded simultaneously with membrane currents and potential. To assess the effects of DPA on the electrical properties of the muscle fiber, we compared the properties of capacitive currents before and after the addition of DPA to the bath. A typical example of current records acquired under control conditions in response to a family of depolarizing and hyperpolarizing pulses (10 ms duration) are shown in the top panels of Fig. 5 A. The bottom traces of Fig. 5 A show that the corresponding fluorescence records remain flat during the pulses, demonstrating that ECFP-F fluorescence, per se, is insensitive to depolarizations and hyperpolarizations to membrane potentials spanning the range from −150 to +50 mV. The addition of 5 μM DPA has visible effects on the current records and generates QRET signals in the optical records, as illustrated in Fig. 5 B. For depolarizing pulses, capacitive currents display a notorious enhancement of a slow decay component (top left panel) that was relatively small in records obtained under control conditions (Fig. 5 A); this is compatible with the presence of a drug-induced increase in the total membrane capacitance of the cell. For example, before DPA exposure, the relaxation kinetics of the capacitive transient elicited by a depolarizing pulse to +10 mV could be fitted to a double exponential function with I_1, τ_1 and I_2, τ_2 values of 0.97, 0.34 and 0.13, 2.49 (mA/cm², ms), respectively. These values changed to 1.28, 0.33 and 0.4, 2.46 (mA/cm², ms), respectively, after DPA, reflecting the enhancement of the slow component linked to an

increase in the cell capacitance from 6.3 to 10 $\mu F/cm^2$ ($\sim$60% increase). In contrast, the effects of DPA on capacitive transients elicited by hyperpolarizing pulses were negligible. A comparative analysis of QRET traces shows a marked asymmetry between the relatively large QRET transients elicited by depolarizing pulses (bottom left) and the small changes observed in the hyperpolarizing direction (bottom right). For example, the $\Delta F/F$ amplitude of the QRET signal elicited by a depolarizing pulse to +10 mV signal was $\sim -4.3\%$ whereas that one elicited by an identical pulse in the opposite direction (to −190 mV) was $\sim +0.7\%$. It should be noted that the ample nonlinear increase in the amplitude of the signals with the magnitude of depolarizing pulses contrasts with the crowding of QRET transients observed in response to hyperpolarizing pulses. It is also apparent that the asymmetry observed in the QRET records has an electrical equivalence since the total capacitive charge (measured by integration of the current) for a depolarizing 100-mV pulse (Fig. 5 B, top, blue trace) was 1.2 $\mu C/cm^2$, which contrasts with the 0.63 $\mu C/cm^2$ for the hyperpolarizing pulse of the same magnitude. Also, the rising phase of QRET records obtained with depolarizing pulses display faster kinetics ($\tau < 1.3$ ms) than the slow time constant of decay of the corresponding capacitive transients ($\tau_2 \sim 2.4$ ms). We will show later that this discrepancy is compatible with the predictions by a radial cable model of the TTS, where we believe the majority of the QRET signals originate.

The results presented so far are in general agreement with the idea that DPA translocates from the outer to the inner leaflet of the TTS membrane in a voltage-dependent manner; this enables the FRET interaction between fluorescence proteins anchored to the inner leaflet of the membrane and DPA, hence the QRET signal. An important consequence of this model is that at the steady state there should be a correspondence between the electrical manifestation of the DPA translocation and the voltage-dependent magnitude of the optical records. To further investigate this point, we first measured Q at the onset and at the end of every voltage pulse and then plotted them against the membrane potential for the same fiber of Fig. 5. The results obtained in the absence of DPA are shown in Fig. 6 A (filled squares) superimposed with those in the presence of 5 μM DPA (open and filled circles). It can be observed that without DPA, the dependence of Q on the membrane potential is approximately linear as expected for a capacitor, except for a small fraction of nonlinear charge movement component (see below). Nevertheless, the addition of DPA introduced a substantial nonlinear component in the current records, which is manifested as a voltage-dependent excess charge ΔQ (note the deviation from linearity of the data in Fig. 6 A). The magnitude of the DPA charge contribution can be better estimated by subtracting the data recorded before DPA addition (linear regression in Fig. 6 A), from those obtained after the addition of DPA, and plotting the difference as a function of the membrane potential (Fig. 6 B). This plot clearly illustrates the marked asymmetry between the DPA electric charges mobilized by pulses in the depolarizing direction from the HP of −90 mV, when compared with those by hyperpolarizing pulses. As shown previously in other preparations (Benz et al., 1976; Fernandez et al., 1983; Gonzalez and Tsien, 1995), the voltage dependence of the translocation of the excess charge (ΔQ) of a lipophilic anion across the lipid bilayer can be predicted by a single barrier (two-state) model. At the steady state, ΔQ at any given membrane voltage (V_m) is given by the Boltzmann expression

$$\Delta Q = \Delta Q_{max}\left(\frac{1}{1+e^{\frac{-\alpha F(V_m - V_h)}{RT}}} - \frac{1}{1+e^{\frac{-\alpha F(HP - V_h)}{RT}}}\right), \quad (4)$$

where ΔQ_{max} ($\mu C/cm^2$) is the total charge available to be moved (in this fiber 0.96 $\mu C/cm^2$), V_h (mV) is the voltage at which half of the total charge is at each state across the barrier (+8 mV for this fiber), α is the fraction of the electric field sensed by the mobile charge (0.84 for this fiber), HP (mV) is the holding potential, and F, R, and T have their usual meaning. The adequate fit of Eq. 4 to the data (Fig. 6 B, continuous curve) demonstrates that the DPA contribution to the current records broadly satisfies the expectations for the translocation of charges across the muscle membranes. An expected consequence of this charge translocation is that the capacitance (C_m) of the muscle fiber should be incremented by a voltage-dependent component. This is illustrated in Fig. 6 C. Before the addition of DPA (filled squares), the capacitance (obtained by dividing the current integral Q by the magnitude of the pulse) showed a relatively constant value typical of a linear capacitor, except for small voltage-dependent contributions given by the presence of voltage-dependent charge movements related to the excitation–contraction coupling and the gating of ion channels intrinsic to the muscle fibers (Schneider and Chandler, 1973; Simon and Beam, 1985a; Delbono et al., 1991; Kim and Vergara, 1998a). Overall, these charge movement contributions account for up to 25% deviation from a constant value of the recorded C_m as they are activated by both hyperpolarizing and depolarizing pulses from the HP (Adrian et al., 1976; Brum and Rios, 1987). In the case of the fiber in Fig. 6 C, the maximal contributions to C_m from these sources were estimated to be 20 and 10% in the depolarizing and hyperpolarizing directions, respectively. In contrast, the addition of DPA to the bath results in a significant increase in voltage-dependent capacitance (Fig. 6 C, open circles), which overwhelms the endogenous components. In the presence of DPA, we calculated the overall nonlinearity

TABLE II

Properties of Voltage-dependent Charge Displacement and Capacitance in Mammalian Skeletal Muscle Fibers

Experiment	Fiber radius	ΔQ_{max}	V_h	α	C_0	C_V	V_h	α	C_V/C_0
	μm	*μC/cm²*	*mV*		*μF/cm²*	*μF/cm²*	*mV*		%
				[DPA] = 5 μM					
020706-B	29	0.60	26.33	0.63	4.18	2.59	15.00	0.64	62%
021306A	30	0.96	8.00	0.84	6.11	5.37	30.00	0.62	88%
071706-A	25	0.89	−6.96	0.90	6.24	5.40	44.03	0.41	86%
091906-A	26	1.02	10.37	1.01	6.00	8.14	30.00	0.57	136%
013106-A	32	2.01	−20.00	0.60	6.74	6.02	20.00	0.50	89%
033006-D	30	0.64	−2.61	0.79	6.83	3.36	46.30	0.46	49%
Mean ± SEM	28.7 ± 1.1	1.0 ± 0.2[a]	2.5 ± 6.5[a]	0.8 ± 0.06	6.0 ± 0.4[a]	5.2 ± 0.8[a]	30.9 ± 5.1[a]	0.54 ± 0.04	85 ±12%[a]
n	6	6	6	6	6	6	6	6	6
				[$DiBAC_4(5)$] = 5 μM					
020806-AJ	26	0.23	5.69	0.72	5.35	2.0	49.8	0.43	37%
020806-E	27	0.64	−2.61	0.79	6.83	3.4	46.30	0.46	49%
071406-B	25	1.31	−11.03	0.83	6.09	6.9	28.58	0.57	113%
Mean ± SEM	26 ± 0.6	0.73 ± 0.2[a]	−2.7 ± 3.4[a]	0.8 ± 0.03	6.1 ± 0.3[a]	4.0 ± 1.2[a]	41.4 ± 4.6[a]	0.5 ± 0.03	66 ± 17%
n	3	3	3	3	3	3	3	3	3
Experiment	Fiber radius	ΔQ_{max}	V_h	κ	C_0	C_{max}	V_h	κ	C_{max}/C_0
	μm	*μC/cm²*	*mV*	*mV*	*μF/cm²*	*μF/cm²*	*mV*	*mV*	%
				Controls (without hydrophobic ions)					
020206-A	28	0.15	−13.86	11.8	4.93	1.33	8.77	20.27	27%
020106-F	27	0.22	−40.00	20	4.58	0.49	−29.28	20.00	11%
082806-A	23	0.14	−20.90	8.6	4.04	1.47	14.12	27.84	36%
021306-A	32	0.07	−20.05	12.5	5.48	1.51	10.91	25.00	28%
020706-EJ	27	0.13	−28.4	17.9	5.23	1.69	13.79	35.16	32%
Mean ± SEM	27.4 ± 1.4	0.14 ± 0.02[a]	−23.7 ± 3.6[a]	13.3 ± 1.5	4.8 ± 0.2[a]	1.2 ± 0.2[a]	1.1 ± 6.8[a]	23.3 ± 1.3	25 ± 4%[a]
n	5	5	5	5	5	5	5	5	5

The Boltzmann expressions used to calculate parameters for voltage-dependent charge translocation and capacitance increase were Eqs. 4 and 5, respectively. For the endogenous charge movements (controls), the argument of the exponential functions was $-(V - V_h)/\kappa$, instead of $-\alpha F/RT(V - V_h)$ because the valence of the mobile charge is undetermined.

[a]Significance with respect to the respective control at the Student $P < 0.05$ level.

by fitting the data (represented by the open circles) to the equation

$$C_m = C_0 + \frac{4C_V e^{\frac{-\alpha F(V_m - V_h)}{RT}}}{\left(1 + e^{\frac{-\alpha F(V_m - V_h)}{RT}}\right)^2}, \quad (5)$$

where C_V (μF/cm²) is the maximal voltage-dependent component of the capacitance, C_0 (μF/cm²) is the voltage-independent capacitance of the cell (measurable at very negative potentials at which the DPA contributions are minimized), V_h is the voltage at which the voltage-dependent capacitance is maximal, and the other parameters were as described above for the Boltzmann expression. Eq. 5, which follows the general definition of capacitance C = dQ/dV (Fernandez et al., 1983), is the explicit derivative of Eq. 4 with respect to the membrane potential plus the voltage-independent component C_0. Fitting Eq. 5 to the data in Fig. 6 C yielded values of 6.1 μF/cm², 5.4 μF/cm², 0.57, and 30 mV for C_0, C_V, α, and V_h, respectively; the resulting curve is shown in the red solid line. Thus, the maximal voltage-dependent component of the capacitance relative to the capacitance at −190 mV grew from ∼9% before DPA staining to 5.4/6.1 = ∼89%, an 80% increase. It can be observed that DPA does contribute with a small percentage increase to the capacitance of the cell at negative potentials, in this fiber 0.3/5.8 = ∼5%, but this is negligible compared with that in the depolarizing direction.

The analysis of voltage-dependent charge movement and capacitance measurements in several fibers, and at various experimental conditions, are summarized in Table II. In general, since it was not required to calculate them before and after DPA addition, as illustrated for the experiment in Fig. 6, the table presents values for the Boltzmann parameters from independent fits to charge and capacitance data in the presence of DPA and $DiBAC_4(5)$ (see below), and include results from control fibers for comparison. From the table, it becomes clear that the fibers' exposure to 5 μM DPA results in significant increases in ΔQ_{max} from 0.14 ± 0.02 μC/cm² in

control fibers to 1.0 ± 0.2 μC/cm^2. This excess charge movement results in an effective increase in membrane capacitance such that the ratio between the capacitance at large depolarizations with that at very negative potentials (C_v/C_0) significantly increases from 25% in control fibers to 85% in fibers with DPA. It should be noted that the capacitance at negative potentials is moderately, though significantly, increased by DPA. It is also clear from Table II that the midpoint of the Boltzmann distribution for the endogenous charge movement is significantly more negative (−23.7 ± 3.6 mV) than that in the presence of DPA (2.5 ± 6.5 mV). This result highlights mechanistic differences between both charge movement processes; this prompted us to identify the slope of the Boltzmann distribution in control fibers with the parameter κ, instead of α used for DPA experiments, which allows for comparison with other reports using the drug in other preparations (Fernandez et al., 1983; Oberhauser and Fernandez, 1995; Chanda et al., 2005). Also, our average value of 13.5 ± 2.1 mV for κ evidences that the endogenous charge movement in mammalian muscle fibers involves the translocation of multiple charges (Simon and Beam, 1985b; Delbono et al., 1991; Collet et al., 2003). Another interesting feature of the data in Table II is that the values of V_h obtained from fits to the DPA-induced nonlinear charge movement (2.5 ± 6.5 mV) are significantly more negative than the value at which the voltage-dependent capacitance reaches its maximum (30.9 ± 5.1 mV). For cells with a single membrane compartment, these values should coincide (Fernandez et al., 1983). The discrepancy reported in Table II could be explained if the voltage-dependent capacitance induced by DPA in muscle fibers arises mostly from current contributions generated in a membrane compartment where the voltage is not uniform. This possibility is supported by model simulations of the electrical behavior of the TTS, as presented in the Discussion.

An obvious expectation is that QRET transients such as those shown in Fig. 5 B (bottom panels) and Fig. 7 A should display a voltage dependence that mirrors that of the charge translocation. To verify this, we calculated the average amplitude of QRET transients during a 2-ms time interval (dotted rectangle in Fig. 7 A) and plotted it as a function of the membrane potential (Fig. 7 B). Optical data were fitted to a Boltzmann distribution and the resulting $\Delta F/F_{max}$, V_h, and α were −0.13, −7.2 mV, and 0.7, respectively. These voltage-dependent parameters were consistent with those found for the charge displacement data in Fig. 7 C, where Q_{max}, V_h, and α were 0.9, −7.0, and 0.9, respectively. The similarity between both datasets is illustrated in the superimposed plots displayed in Fig. 7 D, thus demonstrating that the majority of the charge movement recorded in the presence of DPA gives rise to the QRET signals. This is to be expected since the charge transfer across the lipid bilayer in response to depolarizing pulses merely increases the probability of DPA molecules to be in close proximity of ECFP-F fluorophores such that energy transfer occurs and manifest itself as a QRET signal. In contrast, hyperpolarizing pulses can generate charge mobilization which, due to the steep nonlinearity FRET, does not result in detectable optical changes.

Voltage-dependent FRET between EGFP-F and an Oxonol Dye

We have demonstrated so far that DPA can be used as a voltage-dependent quencher of the ECFP-F (or EGFP-F) fluorescence in order to elicit QRET signals in muscle fibers. It seemed interesting to explore whether fluorescent (rather than absorber) mobile lipophilic ions could be used to generate FRET pairs with these fluorescent proteins. To this end, we chose the oxonol dye $DiBAC_4(5)$ whose absorbance spectrum has significant spectral overlap with the emission of EGFP-F (Fig. 8 A), thus making it a good candidate for FRET-based measurements of TTS membrane potential changes; the calculated R_o for this pair was 3.8 nm. Muscle fibers expressing EGFP-F were stained with 5 μM $DiBAC_4(5)$ dissolved in suitable external solutions and voltage-dependent optical signals were studied in both current- and voltage-clamp conditions as described above for DPA experiments. As illustrated in Fig. 8 B, AP stimulation elicits two voltage-dependent optical signals of opposite sign: (a) one displaying the reduction in EGFP-F fluorescence due to the enhanced FRET absorbance by oxonol molecules ("donor quenching," Fig. 8 B, top left) and (b) the other representing the increase in $DiBAC_4(5)$ fluorescence due to the enhanced fluorescence excitation of $DiBAC_4(5)$ by EGFP-F ("acceptor sensitized emission," Fig. 8 B, top right). It can be observed that the absolute magnitude of the optical transients (ΔF/F) differ largely; however, when the signals are scaled to match their amplitudes, it is evident that they are kinetically identical (unpublished data). More importantly, in contrast with the results obtained with DPA, the optical transients obtained with the EGFP-F//$DiBAC_4(5)$ pair are significantly slower than the AP, suggesting that this FRET pair has a lower frequency response than those based on DPA translocation. It should be noted that the sensitized acceptor fluorescence transient (Fig. 8 B, red trace) displays an excellent s/n ratio and a peak ΔF/F of ∼28%, significantly larger than AP-elicited QRET transients recorded with DPA (Fig. 4).

Optical signals obtained under voltage-clamp conditions are shown in Fig. 8 C. As expected, donor quenching transients exhibit negative ΔF/F for depolarizations (and positive ΔF/F for hyperpolarizations), whereas acceptor-sensitized emission transients had the opposite sign. Also, in agreement with the observations with DPA, the amplitude of both the quenching and the sensitized emission transients show a nonlinear voltage dependence as expected from signals that originate from charge

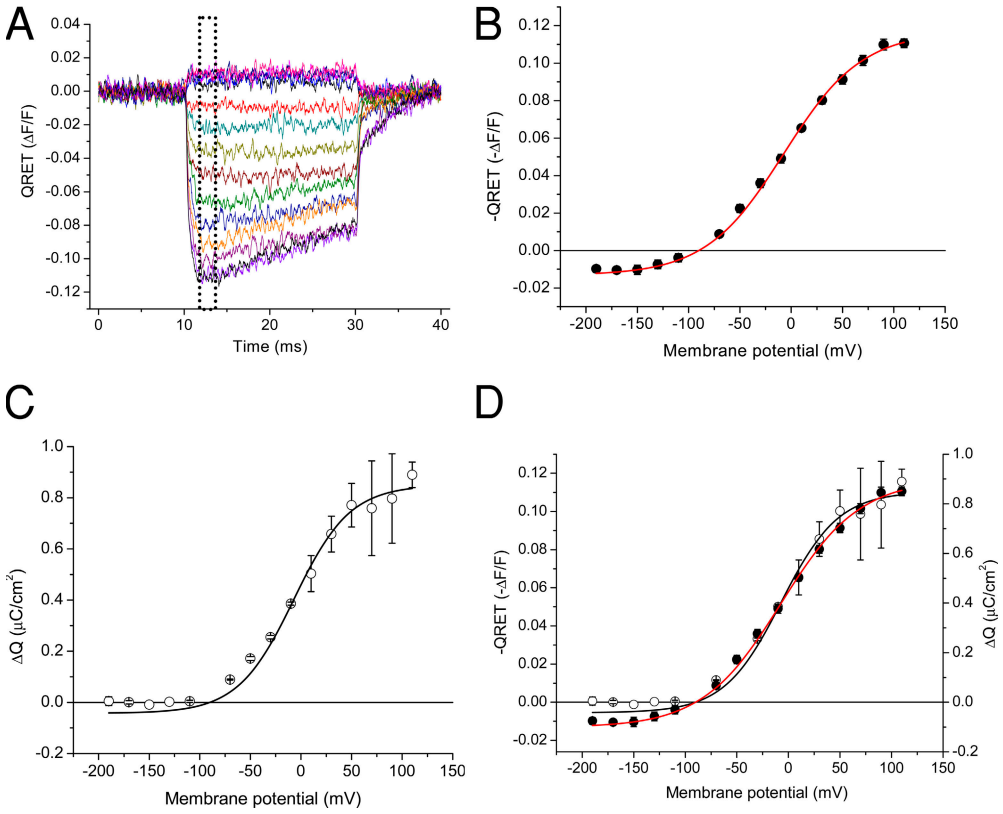

Figure 7. Voltage dependence of the FRET interaction between ECFP-F and DPA. (A) QRET transients (ΔF/F) recorded in response to 20-ms voltage steps. The pulses were ±20, ±40, ±60, ±80, ±100, 120, 140, 160,180, and 200 mV. QRET transient amplitudes were measured as the average amplitude during a 2-ms interval, 2 ms after the onset of the pulses (indicated by the dotted rectangle). (B) Voltage dependence of the average QRET amplitude (filled circles). The error bar is the SD of the noise. Note that the ordinate is in −ΔF/F units. The solid line represents the adjustment of the data to a Boltzmann distribution. (C) Extra charge contributed by DPA (on and off average) is shown in open circles. The error bars of the data points represent the SEM of on and off averages. The solid line corresponds to the adjustment of the data to a Boltzmann distribution. (D) Superimposition of average QRET transient and charge data, including adjusted curves. See text for details.

translocations across the membrane. Namely, at either wavelength range, hyperpolarizing pulses elicited very small signals when compared with those elicited by depolarizing pulses of the same magnitude (i.e., compare cyan and magenta traces, elicited by −100 and +100-mV pulses, in the top and bottom panels of Fig. 8 C). Another feature of the FRET records in Fig. 8 C is that the ΔF/F changes in $DiBAC_4(5)$ fluorescence (Fig. 8 C, bottom) are significantly larger, and consequently display a better signal-to-noise (s/n) ratio, than the corresponding donor quenching transients (Fig. 8 C, top). However, the superposition of appropriately scaled donor and acceptor FRET traces nearly matches each other's kinetics, except for secondary distortions due to experimental variations between individual traces and experimental noise (unpublished data). The close matching between donor and acceptor transients is further confirmed by steady-state data as shown in Fig. 8 D. The voltage-dependent amplitude of the donor fluorescence signals (closed circles) nearly mirrors that one of the acceptor fluorescence signals (open circles). The adjustment of the data to Boltzmann distributions (green and red sigmoidal curves for donor and acceptor signals, respectively) demonstrates almost identical slope parameters (α = 0.7 and 0.74 for donor and acceptor curves, respectively) and similar mid-voltages (V_h = 0 and 15 mV, respectively). The asymptotes of the fitted curves (in ΔF/F) were −0.09 and 0.6 for donor and acceptor data, respectively; the difference in amplitudes highlights the major improvement in optical efficacy (6.7-fold) that can be attained by alternative fluorescence detection protocols while sharing the same FRET mechanism. It is interesting that the fractional ΔF/F amplitudes of the donor quenching signals with the EGFP-F//$DiBAC_4(5)$ pair is not dissimilar to that of EGFP-F//DPA QRET signals, which is consistent with the similarity in their R_0 values (3.8 and 3.7 nm, respectively). However, in spite of the advantages of the EGFP-F//$DiBAC_4(5)$ hybrid pair in terms of the improved signal-to-noise that can be attained with the red fluorescence, and the possibility to generate ratiometric signals, it is clear that they display more kinetic limitation than QRET signals. For example, the rising time constant of the traces elicited by depolarizing pulses in Fig. 8 C is ∼2.2 ms, compared with the ∼1.3 ms of QRET signals. We will show later that this is due to a slower voltage-dependent translocation of $DiBAC_4(5)$ ions, than that of DPA, across the TTS membranes. However, as noted in the data presented in Table II, the steady-state contribution of $DiBAC_4(5)$ to the overall charge translocation (in μC/cm²) and to the voltage-dependent increase in capacitance (in μF/cm²) is not significantly different than that of DPA.

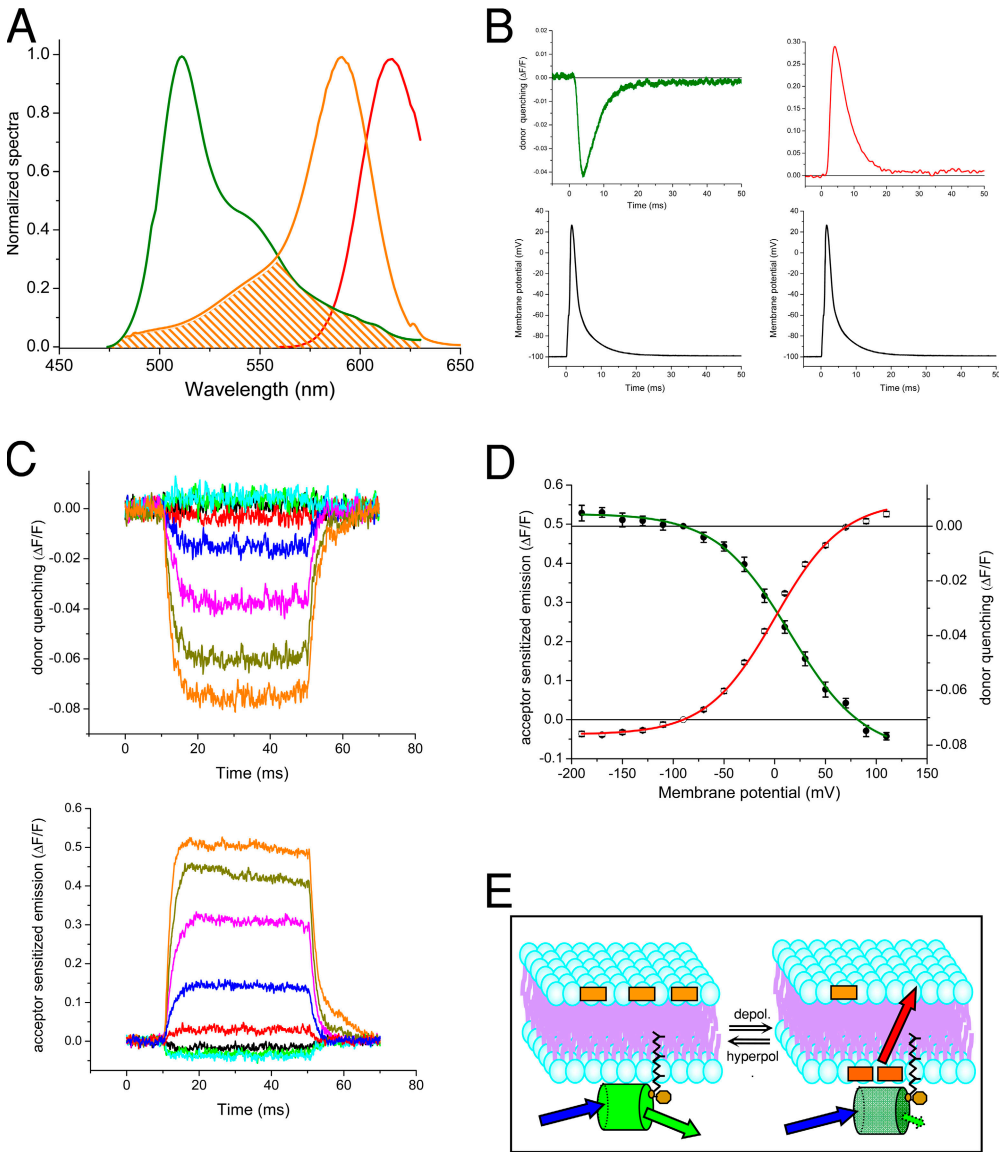

Figure 8. Dynamic FRET signals between DiBAC$_4$(5) and EGFP-F. (A) EGFP-F emission spectrum (green trace) was measured in vivo and DiBAC$_4$(5) absorption (orange trace) and emission (red trace) spectra were measured in vitro. They were plotted normalized for comparison. The orange dashed area represents the region of spectral overlap between the EGFP-F emission and DiBAC$_4$(5) absorbance. (B) Fluorescence changes (top) elicited by two consecutive AP stimulation (bottom) recorded from a fiber expressing EGFP-F and stained with DiBAC$_4$(5). Donor quenching (green trace) and acceptor-sensitized emission (red trace) are presented in the left and right panels, respectively; and were acquired consecutively by switching from the donor-EGFP to the sensitized-DiBAC$_4$(5) filter sets (Table I). (C) The top and bottom panels show the EGFP-F and the DiBAC$_4$(5) fluorescence changes elicited by 40-ms voltage pulses of ±20, ±60, ±100, 140, and 180 mV. The entire sequence of transients (applied at intervals of ~1 min) was recorded first with the "donor-EGFP" cube and then with the "Sensitized-DiBAC" cube. Control records were obtained afterwards by alternating cubes for the same pulse amplitude (not depicted). (D) Voltage dependence of donor FRET (filled circles) and acceptor FRET (open circles). Signal amplitude was measured from averages during a 2-ms interval, measured 5 ms after the onset of the pulses. The error bar indicates the SD of the noise. Solid lines are Boltzmann fitting to the data. The characteristic parameters ($\Delta F/F_{max}$, κ, and V_h) for the green/red sigmoidal curves were −0.09/0.6, 36.4/33.6 mV, and 15/0 mV, respectively. (E) Schematic model of the voltage-dependent translocation of DiBAC$_4$(5) underlying its FRET interaction with EGFP-F. Different colors and length of the arrows highlight the wavelength of excitation of EGFP-F, and the change in fluorescence intensity of EGFP-F and DiBAC$_4$(5).

DISCUSSION

In this paper we describe the first time use of FRET-based methods to measure membrane potential changes at the TTS system in mammalian skeletal muscle fibers. The method takes advantage of the ability of mammalian muscle to effectively express transgenic proteins in response to in vivo electroporation of DNA plasmids.

It had been previously demonstrated that muscle tissue can efficiently express recombinant soluble fluorescent proteins (e.g., EGFP and ECFP) following transfection of plasmids under the control of the CMV promoter (Dona et al., 2003; Umeda et al., 2004; DiFranco et al., 2006). Our current results demonstrate that muscle fibers can also efficiently express EGFP and ECFP constructs carrying a farnesylation signal; low magnification images show that up to 80–90% of the FDB muscle fibers were transfected (unpublished data). Most importantly, skeletal muscle fibers seem to provide the precise enzymatic environment to ensure that farnesylation occurs and that the EGFP-F and ECFP-F proteins are subsequently targeted to external membranes (surface and TTS membranes). These are critical features for an efficient hybrid FRET-based system since low amounts of fluorescent protein dissolved in the myoplasm (or associated with internal membrane compartments) ensure low background

fluorescence and large signal-to-noise ratios in the optical data. Although EGFP-F and ECFP-F seem to be similarly targeted to both the surface and TTS membranes (Fig. 2), the FRET hybrid system reported here has the potential to be adapted for specific marker signals capable of differentially directing the expression of membrane proteins either to the TTS or the surface membrane. This would allow independent studying of these membrane compartments with standard light detection techniques, a goal previously approached by invasive detubulation procedures (Gage and Eisenberg, 1967; Heiny and Vergara, 1982).

QRET and FRET Signals Arise mostly from the TTS Membranes

It is well established that the electrical properties of muscle fibers are determined not only by the surface membrane but they reflect the important contributions from the TTS, which is a radial cable network connected to the surface membrane (Falk and Fatt, 1964; Adrian et al., 1969; Adrian and Peachey, 1973; Ashcroft et al., 1985; Kim and Vergara, 1998b). Thus, it seemed important to analyze whether radial cable model simulations of the muscle fiber (see Appendix) were able to predict the effects of DPA (and of $DiBAC_4(5)$) observed in the electrical records and if they provide a way to interpret the optical signals. As shown in the Appendix, we incorporated the kinetic equations of the two-state model for the voltage-dependent translocation of hydrophobic ions (Fernandez et al., 1983; Gonzalez and Tsien, 1995) to the surface and TTS membranes and computed the model predictions for capacitive currents and charge translocation by numerical integration of the partial differential questions using an implicit algorithm (Heiny et al., 1983; Ashcroft et al., 1985; Kim and Vergara, 1998b). The results of model simulations shown in Fig. 9 aimed specifically at predicting the data in Figs. 5 and 6, but were equally successful in fiber-to-fiber comparisons. Fig. 9 (A and D) shows data and model predictions, respectively, for the total charge translocation obtained in response to voltage-clamp pulses in a muscle fiber with and without DPA. It can be observed that model predictions (Fig. 9 D) are in good agreement with the experimental data obtained before and after the addition of DPA. Also, the model traces simulated in response to a 10-ms, +10-mV pulse are shown in the inset of Fig. 9 D to illustrate their similarity, both in amplitude and kinetics, to typical experimental records obtained with the same voltage. The deviations from the predictions can be mostly attributed to the absence in the model of endogenous nonlinear charge movements that are responsible for slow components (albeit small) in the experimental current records. An important piece of information that we aimed to get from the kinetics of the capacitive transients was what actual rate of DPA translocation across the TTS and surface membranes consistently predicts the experimental observations. We found that a value of ~0.6 ms for the maximal voltage-dependent time constant (τ_{max}) yielded adequate predictions of the observed decay in experimental capacitive transients, i.e., 0.3 mA/cm^2 and 2.14 ms for I_2 and τ_2, respectively, for a pulse to +10 mV (see text and Fig. 5). Smaller or larger values of τ_{max} resulted in transients either too slow or too fast compared with the data. Our value of 0.6 ms for DPA translocation is almost identical to that reported for optical signals in other preparations (Chanda et al., 2005) but approximately twice as long as that obtained from impedance measurements in the squid giant axon (Fernandez et al., 1983). What is interesting is that the slowing down of the capacitative transients observed in muscle fibers appears to be amplified by the delocalized contribution from the TTS.

Model simulations are also important to quantitate the steady-state properties of charge translocation, which must be assigned to the TTS in order to predict the actual experimental observations from the fibers. We found that the data in Fig. 9 B was well predicted by model simulations using values of 0.5 μC/cm^2, 8 mV, and 0.84 for ΔQ_{max}, V_h, and α, respectively. The values of V_h and α for the Boltzmann fit to Eq. 4, shown in Fig. 9 E, are identical not only to the above values, but also to those from the fits to the experimental data (Fig. 9 B). The interesting prediction is that the translocation of a maximum of 0.5 μC/cm^2 across the surface and TTS membranes accounts for the larger value of 0.99 μC/cm^2 observed in the overall fiber, clearly demonstrating that the effects of DPA are magnified due to its presence in the TTS. An exciting feature of model predictions is that, as shown in the insert of Fig. 9 E, both the marked asymmetry and the kinetics of QRET signals are well predicted by the kinetics of the voltage-dependent component of charge translocation in response to pulses to −190 and +10 mV. The main reason for the relatively fast kinetics of the observed and predicted traces, with respect to that of capacitive transients, is that optical signals arise from multiple radial components of the TTS and surface membranes whose relative contributions can be accounted for by a radial dependence in the computed ensemble average calculation (Ashcroft et al., 1985; Kim and Vergara, 1998b).

Another important property of the muscle fibers that could only be accounted for by the participation of the TTS in the DPA effects is the capacitance increase. As seen in Fig. 9 (C and F), model simulations readily predict that DPA increases the membrane capacitance of the muscle fiber in a voltage-dependent fashion from ~6 μF/cm^2 in the absence of the drug to ~12 μF/cm^2 in its presence; the model also predicts the peculiar shift of V_h, by ~30 mV to more positive potentials, for the capacitance increase with respect to that for the charge redistribution. It should be highlighted that the geometrical properties of the TTS for this particular fiber

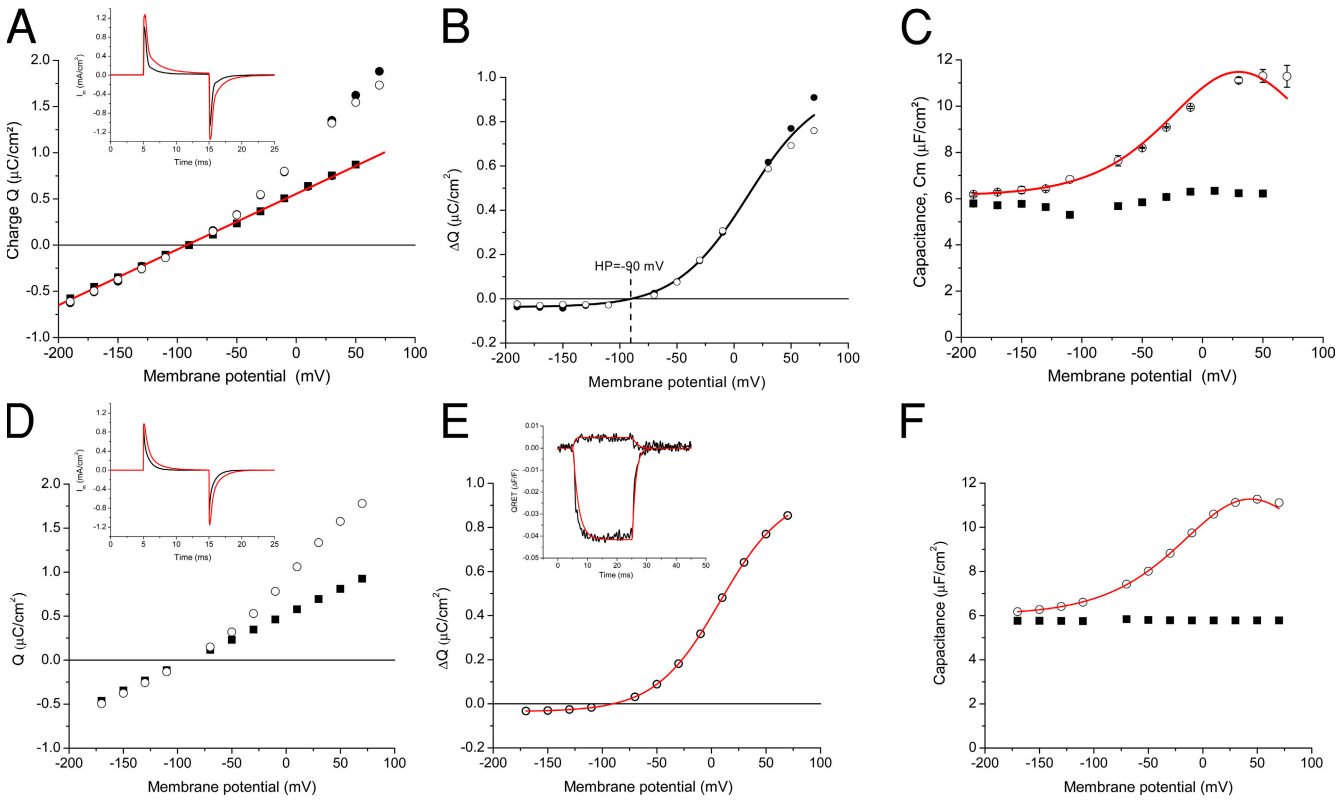

Figure 9. Model predictions of charge and capacitance contributed by DPA. A–C are the same as in Fig. 6. D–F are model predictions of the data in A–C, respectively. (D) The data points are the total charge in the absence (closed squares) and in the presence of DPA (open circles). The insets in A and D are capacitive currents obtained in the presence (red traces) and in the absence of DPA (black traces) in response to 10-ms pulses to +10 mV. (E) Predictions of the net charge contributed by DPA. The solid line is a Boltzmann fit to the simulated data. The inset shows QRET transients (in black) obtained in response to 10-ms pulses to +10 mV (downward trace) and −190 mV (upward trace). The modeled data (solid red traces) were computed as the ensemble average of the net translocated charge in response to the same pulses. The amplitude of the modeled traces were scaled and inverted in order to match the largest ΔF/F of the data in response to the pulse to +10 mV. Note that the asymmetry between negative and positive pulses is a model prediction. (F) Cell capacitance in the absence (filled symbols) and in the presence of DPA (open circles). Note that the capacitance under control conditions is not voltage dependent (the model lacks of endogenous nonlinear charge). The solid line is the fit of the model results to Eq. 5 (see text), yielding 6.1 μF/cm², 5.1 μF/cm², 0.64, and +35 mV, for C_0, C_V, α, and V_h, respectively. The rest of the parameter values for the radial cable model simulations are in Table III of Appendix; also, see Discussion.

account for both the control and DPA values. There are deviations from the data since endogenous voltage-dependent capacitive components were not included in model simulations; but as illustrated in Table II, the effects of DPA in the membrane capacitance dominate over endogenous components.

The comparison of model predictions with FRET data obtained with the oxonol dye $DiBAC_4(5)$ using the same approach outlined above for DPA data yields very comparable parameters for the charge translocation process, with the exception that the τ_{max} necessary to reproduce the kinetics of capacitive transients and FRET signals was 1.6 ms, instead of the 0.6 ms for DPA. These observations confirm previous reports that oxonol dyes undergo slower voltage-dependent translocations and FRET signals (in the range of 3–10 ms) than DPA (Gonzalez and Tsien, 1995, 1997; Chanda et al., 2005). However, our observations in skeletal muscle fibers seem to suggest that $DiBAC_4(5)$ may be particularly faster than other oxonol probes.

QRET and FRET Mechanisms

Our data provide an exhaustive characterization of the voltage-dependent charge translocation that must be inherently linked to the genesis of QRET and FRET signals. It should be noted that for all the filter combinations used (Table I), the muscle fibers' autofluorescence was negligible and was not affected by the exposure to DPA. We also verified that when tested alone each component of the QRET and FRET pairs do not display significant voltage-dependent changes in their fluorescence. Thus, as shown in Fig. 3, in the absence of a fluorescence acceptor such as DPA (or $DiBAC_4(5)$), EGFP-F's fluorescence does not exhibit detectable sensitivity to membrane potential changes. The same is valid for ECFP-F (unpublished data). Also, in control experiments we measured

voltage-dependent fluorescence changes of <0.5% ΔF/F in fibers stained with $DiBAC_4(5)$. These are negligible values compared with the ΔF/F of the data shown in Fig. 8, demonstrating that within the time scale of our experiments the potentiometric response of $DiBAC_4(5)$ alone does not contribute to our FRET signals. This is not surprising since the features of this (and other oxonol) potentiometric indicator depend on the net transport of dye molecules across the membrane, which take minutes to equilibrate (Loew, 1993). The results reported here in skeletal muscle fibers confirm previous information from other preparations demonstrating a significant speed enhancement in the voltage-dependent response when this type of indicator is coupled with membrane-resident molecules to generate FRET-based reporters (Gonzalez and Tsien, 1995, 1997; Gonzalez and Maher, 2002). Extending the observations of these authors, we show here the feasibility of using genetically encoded fluorescence proteins to generate not only QRET signals (with DPA), as reported previously (Chanda et al., 2005), but also bonafide FRET signals with $DiBAC_4(5)$, which display symmetrical matching features at the donor and acceptor wavelengths, making it an excellent choice for ratiometric measurements (Tsien et al., 1993).

We showed that the peak ΔF/F amplitude of AP-evoked QRET signals recorded with the novel ECFP-F protein was 7.1 ± 0.5%, whereas a value of 3.6 ± 0.8% was obtained with EGFP-F (Fig. 4), reflecting a nearly twofold difference in efficiency. Such an increase in QRET efficiency would be expected from the larger spectral overlap between ECFP-F and DPA as compared with that of EGFP-F and DPA. From theoretical calculations for randomly oriented donors and acceptors in the membrane, it can be inferred that the ratio of FRET efficiency for two FRET pairs with $R_0^1 > R_0^2$ is between 1 and $(R_0^1 / R_0^2)^6$ (Shaklai et al., 1977; Dewey and Hammes, 1980). Nevertheless, if published quantum yield values ($\Phi_{ECFP} = 0.4$, $\Phi_{EGFP} = 0.6$; see Patterson et al., 2000) were to be used to calculate R_0s for both pairs, and the maximal ratio of energy transfer (Shaklai et al., 1977; Dewey and Hammes, 1980) was computed according to the approximation

$$\left(\frac{R_0^{ECFP//DPA}}{R_0^{EGFP//DPA}}\right)^6,$$

a value of 1.54 would have been obtained; this is smaller than the observed experimental ratio of ~2. In the search for possible explanations for this discrepancy we hypothesized that the actual values of Φ for EGFP and ECFP might be different than those published. This prompted us to measure Φ using batches of highly purified proteins manufactured by muscle fibers (DiFranco et al., 2006) at multiple protein concentrations and state of the art procedures (based on comparative linear regression analysis) with fluorescein as a standard (Williams et al., 1983; Magde et al., 2002). We obtained a value of 0.6 for Φ_{EGFP} that is identical to the published one, but a value of 0.62 for Φ_{ECFP}, which is significantly larger than the published one (Patterson et al., 2000). Importantly, when these values were used in the calculation of R_0s, the prediction of maximal ratio of FRET efficiency becomes 2.4, which helps to explain the experimental observations.

The above results highlight the importance of the spectral overlap in the efficiency of FRET signals inasmuch it is one of the main factors determining the value of R_0 for the energy transfer process. In further support of this concept, the amplitude of AP-evoked donor quenching transients recorded with EGFP-F//$DiBAC_4(5)$ (Fig. 8 B) are quite similar to that of QRET transients (Fig. 4). The calculated R_0 values for both of these FRET pairs are 3.8 and 3.63 respectively; thus, assuming that the conditions are comparable, the expected ratio of efficiency should be less than

$$\left(\frac{R_0^{EGFP//DiBAC_4(5)}}{R_0^{EGFP//DPA}}\right)^6 \sim 1.32,$$

in agreement with the observed ratio of 0.042/0.036 ~ 1.2.

We showed above that the maximal charge mobilization in the TTS membranes by DPA is 5×10^{-7} Coulombs/cm^2, which is equivalent to a surface density of ~30,000 DPA/μm^2. If we assume that DPA molecules instantly equilibrate at the internal leaflet of membrane, while attaining an equidistant distribution, their average intermolecular distance would be ~6.5 nm. This is a relatively long distance when compared with the R_0 values calculated for both ECFP-F and EGFP-F; in fact the values are not too different from the range in which first order approximation applies and the ratio between ECFP-F//DPA and EGFP-F//DPA transients should approach 2.4. These results concur with the general prediction by Chanda et al. (2005, see Fig. S2 therein) that the QRET signals generated by the translocation of low concentrations of DPA molecules would display larger ΔF/Fs for longer R_0s.

Future Perspectives

The results presented in this paper demonstrate that the voltage-dependent translocation of lipophilic ions across the surface and TTS membranes of the muscle fiber results in enhanced FRET interactions with internally expressed anchored fluorescent proteins due to shortening of their relative distances. This enhancement can be tracked dynamically by monitoring kinetic changes in donor fluorescence quenching and/or acceptor-sensitized emission. Absorber or fluorescent lipophilic ions not only can be used to sense membrane potential changes, but also to investigate the sidedness of particular domains of membrane proteins, or if domain-bearing tags of transmembrane proteins move in response to voltage changes in the TTS.

Consequently, we submit that dynamic FRET methods, as reported here, can be used to study the rapid conformational changes of proteins involved in the voltage-dependent signal transduction, underlying excitation–contraction coupling, that occur at the TTS in mammalian skeletal muscle fibers.

APPENDIX

Numerical Integration of the Radial Cable Model Equations for Mammalian Skeletal Muscle Fibers under Passive Conditions

We followed the nomenclature and procedures reported previously for amphibian muscle fibers (Ashcroft et al., 1985; Kim and Vergara, 1998b) and the assumption (Adrian and Peachey, 1973) that the lumen of the TTS is separated from the extracellular fluid by an access resistance (R_s, in Ωcm^2). The partial differential equation that governs the radial (r) and time (t) dependent changes in T-tubule potential, $u(r,t)$ in response to potential changes at the external boundary is (Adrian et al., 1969)

$$\frac{\partial^2 u}{\partial R^2} + \frac{1}{R}\frac{\partial u}{\partial R} = \nu^2 u + \frac{\partial u}{\partial t}, \tag{A1}$$

where a is the radius of the muscle fiber, $R = r/a$, $T = \bar{G}_L\, t/(\bar{C}_w\, a^2)$ and $\nu = a\sqrt{\bar{G}_w / \bar{G}_L}$. In these equations, the parameters $\bar{C}_w$ and $\bar{G}_w$ are the capacitance (in $\mu F/cm^3$) and conductance (in S/cm^3) of the tubular membrane per unit volume of muscle fiber, respectively, and $\bar{G}_L$ is the effective radial conductivity (in S/cm). If ρ is the fraction of the total muscle volume occupied by T-tubules, σ is a tortuosity factor, and ξ is the volume to surface ratio of the T-tubules, then $\bar{C}_w = C_W\rho/\xi$; $\bar{G}_w = G_W\rho/\xi$; and, $\bar{G}_L = G_L\rho\sigma$, where C_w and G_w are the TTS membrane capacitance (in $\mu F/cm^2$) and conductance (in S/cm^2) per unit surface membrane area, and G_L is the specific T-tubule lumen conductivity (in S/cm).

Numerical integration methods permit a more general approach to investigate the electrical properties of the TTS, and the radial cable equation can be changed in order to take into consideration the possibility that the TTS cable elements are parallel arrangements of nonlinear conductances and capacitances (Adrian and Peachey, 1973; Heiny et al., 1983; Ashcroft et al., 1985). Thus, we start by replacing the term $\partial^2 u$ in Eq. A1 by the more general term:

$$a^2\,\frac{\overline{I_W}(V,r,t)}{\bar{G}_L},$$

where $\overline{I_W}(\mu,r,t)$ is a generalized current through the TTS membrane wall normalized per volume of fiber. Keeping the same definitions for R and T, Eq. A1 is transformed into

$$\frac{\partial^2 u}{\partial R^2} + \frac{1}{R}\frac{\partial u}{\partial R} = a^2\,\frac{\overline{I_W}}{\bar{G}_L} + \frac{\partial u}{\partial t}. \tag{A2}$$

For the simulations in this paper we assumed that $\overline{I_W}(\mu,r,t)$ has resistive and capacitive components given by the equation

$$\overline{I_W}(\mu,r,t) = \bar{G}_W\mu + I_Q(\mu,r,t)\frac{\rho}{\zeta}, \tag{A3}$$

where $I_Q(V, r, t)$ is the nonlinear charge movement current (in this case due to the presence of lipophilic ions) at every radial element of the TTS. Assuming a two-state model of the charge transition (Fernandez et al., 1983; Simon and Beam, 1985a), the following equations apply for every radial element of the TTS:

$$I_Q(\mu,r,t) = \frac{Q_\infty(\mu,r) - Q(\mu,r)}{\tau(\mu,r)} \tag{A4}$$

$$Q_\infty^n(\mu,r) = \frac{Q_{\max}}{1 + e^{\frac{-\alpha F(\mu - V_h)}{RT}}} \tag{A5}$$

$$\tau(\mu,r) = \frac{\tau_{\max}}{\cosh\left(\dfrac{\alpha F(\mu - V_h)}{2RT}\right)}. \tag{A6}$$

The TTS elements are approximated as isopotential concentric shells (s_i, with i ranging from 0 to n) each with voltage u_i. The simulations presented in the text were obtained with $n = 60$ shells; higher number of concentric annuli did not significantly alter the theoretical predictions.

At a given time j, the finite differences approximation of the partial differential equation of the T- tubular voltage is (Crank, 1975)

$$\frac{\partial^2 u}{\partial R^2} + \frac{1}{R}\frac{\partial u}{\partial R} \;\rightarrow\; \frac{1}{2i\,\delta R^2}\left\{(2i+1)\,u_{i+1}^j - 4iu_i^j + (2i-1)u_{i-1}^j\right\},$$

where u_i^j is the finite difference representation of the voltage at radial position i at time j, and δR is the normalized distance between shells. The TTS cable is assumed to be sealed at the center of the muscle fiber, and the approximation used to calculate u_0^j is (Crank, 1975)

$$\frac{\partial^2 u}{\partial R^2} + \frac{1}{R}\frac{\partial u}{\partial R} \;\rightarrow\; \frac{4}{\delta R^2}(u_1^j - u_0^j).$$

The finite differences approximation for the time dependence partial differential operator for an arbitrary cable element u_i^j is

$$\frac{\partial u}{\partial T} \rightarrow \frac{u_i^{j+1} - u_i^j}{\delta T},$$

where δT is the dimensionless time interval. The external boundary condition (R = 1; $i = n$) is (Adrian and Peachey, 1973)

$$\left(\frac{\partial u}{\partial R}\right)_{R=1} = \frac{V_{COM}(t) - u_n^j}{aR_s\bar{G}_L},$$

where $V_{COM}(t)$ is the pulse imposed at the surface membrane of the muscle fiber. The finite differences approximation for this boundary condition is given by

$$\frac{u_n^j - u_{n-2}^j}{2\delta R} = \frac{V_{COM} - u_n^l}{aR_s\bar{G}_L}.$$

Using an implicit Crank-Nicolson algorithm (Crank, 1975; Gerald, 1978), a final finite difference equation for an arbitrary annulus i can be obtained (Kim and Vergara, 1998b):

$$X\cdot\frac{(2i+1)}{4i}\cdot u_{i+1}^{j} - (X+1)\cdot u_i^{j+1} + X\cdot\frac{(2i-1)}{4i}\cdot u_{i-1}^{j+1} =$$
$$-X\cdot\frac{(2i+1)}{4i}\cdot u_{i+1}^{j} + (X-1)\cdot u_i^{j} - X\cdot\frac{(2i-1)}{4i}\cdot u_{i-1}^{j} + a^2\cdot\frac{(\overline{I_W})_i^j}{\overline{G_L}}\delta T,$$

Where $(\overline{I_W})_i^j$ is the current per unit fiber volume flowing through the T-tubular element at shell i and at the time interval j during the numerical integration process and $X = \delta T/\delta R^2$. This is a recursive formula allowing the calculation of u_i^{j+1} at a time interval δT, knowing u_i^j. The system of tridiagonal coefficient matrices was solved using an LU decomposition algorithm (Gerald, 1978). The integration of Eq. A3 to update the value of Q for every cable element was performed with a simple Euler algorithm at every time step. The values of the parameters used for the simulations shown in Fig. 9 are summarized in Table III.

Under the assumption that the optical FRET interaction homogenously occurs at superficial and deep regions of the TTS, and that changes in its optical properties with the transmembrane voltage occur identically at every submicroscopic region of the TTS, then the optical signal obtained under global illumination is expected to represent an ensemble average of the translocated charge in the TTS ($\overline{\Delta Q_{TTS}}$) weighted by the radius of each annulus (Heiny et al., 1983; Ashcroft et al., 1985). This is calculated using a numerical trapezoidal integration algorithm based on Simpson's rule (Gerald, 1978) from the formula

$$\overline{\Delta V_{TTS}} = \frac{\int_0^a rV(r)dr}{\int_0^a rdr}.$$

This assumption was used to calculate the predicted QRET signal (for comparison with the data) in Fig. 9 D.

We thank Drs. R. Blunck, B. Chanda, and F. Bezanilla for the suggestion of using DPA in muscle fibers.

TABLE III

Specific Parameter Values for Passive Radial Model Simulations in Fig. 9

Parameter	Value	Dimension
a	30	μm
C_W	0.9	μF/cm²
G_W	0.3	mS/ cm²
GL	7	mS/cm
R_s	120	Ωcm²
ρ	0.004	
ζ	1.1×10^{-6}	cm
σ	0.5	
Q_{max}	0.5	μC/cm²
V_h	8	mV
α	0.84	
τ_{max} for DPA	0.6	ms
τ_{max} for DiBAC4(5)	1.6	ms

This work was supported by grants from the Muscular Dystrophy Association of America and the National Institutes of Health (AR047664 and GM074706) and a Stein/Oppenheimer Award from University of California Los Angeles.

Edward N. Pugh Jr. served as editor.

Submitted: 23 October 2007
Accepted: 31 October 2007

REFERENCES

Adrian, R.H., and L.D. Peachey. 1973. Reconstruction of the action potential of frog sartorius muscle. *J. Physiol.* 235:103–131.

Adrian, R.H., W.K. Chandler, and A.L. Hodgkin. 1969. The kinetics of mechanical activation in frog muscle. *J. Physiol.* 204:207–230.

Adrian, R.H., W.K. Chandler, and R.F. Rakowski. 1976. Charge movement and mechanical repriming in skeletal muscle. *J. Physiol.* 254:361–388.

Aronheim, A., D. Engelberg, N. Li, N. al-Alawi, J. Schlessinger, and M. Karin. 1994. Membrane targeting of the nucleotide exchange factor Sos is sufficient for activating the Ras signaling pathway. *Cell.* 78:949–961.

Ashcroft, F.M., J.A. Heiny, and J. Vergara. 1985. Inward rectification in the transverse tubular system of frog skeletal muscle studied with potentiometric dyes. *J. Physiol.* 359:269–291.

Bedlack, R.S., M.d. Wei, and L.M. Loew. 1992. Localized membrane depolarizations and localized calcium influx during electric field-guided neurite growth. *Neuron.* 9:393–403.

Benz, R., P. Lauger, and K. Janko. 1976. Transport kinetics of hydrophobic ions in lipid bilayer membranes. Charge-pulse relaxation studies. *Biochim. Biophys. Acta.* 455:701–720.

Benz, R., and W. Nonner. 1981. Structure of the axolemma of frog myelinated nerve: relaxation experiments with a lipophilic probe ion. *J. Membr. Biol.* 59:127–134.

Brum, G., and E. Rios. 1987. Intramembrane charge movement in frog skeletal muscle fibres. Properties of charge 2. *J. Physiol.* 387:489–517.

Chanda, B., R. Blunck, L.C. Faria, F.E. Schweizer, I. Mody, and F. Bezanilla. 2005. A hybrid approach to measuring electrical activity in genetically specified neurons. *Nat. Neurosci.* 8:1619–1626.

Clegg, R.M. 1995. Fluorescence resonance energy transfer. *Curr. Opin. Biotechnol.* 6:103–110.

Collet, C., L. Csernoch, and V. Jacquemond. 2003. Intramembrane charge movement and L-type calcium current in skeletal muscle fibers isolated from control and mdx mice. *Biophys. J.* 84:251–265.

Crank, J. 1975. The Mathematics of Diffusion. Second edition. Oxford University Press, Oxford, UK. 414 pp.

Delbono, O., J. Garcia, S.H. Appel, and E. Stefani. 1991. Calcium current and charge movement of mammalian muscle: action of amyotrophic lateral sclerosis immunoglobulins. *J. Physiol.* 444:723–742.

Dewey, T.G., and G.G. Hammes. 1980. Calculation on fluorescence resonance energy transfer on surfaces. *Biophys. J.* 32:1023–1035.

DiFranco, M., D. Novo, and J.L. Vergara. 2002. Characterization of the calcium release domains during excitation-contraction coupling in skeletal muscle fibres. *Pflugers Arch.* 443:508–519.

DiFranco, M., J. Capote, and J.L. Vergara. 2005. Optical imaging and functional characterization of the transverse tubular system of mammalian muscle fibers using the potentiometric indicator di-8-ANEPPS. *J. Membr. Biol.* 208:141–153.

DiFranco, M., P. Neco, J. Capote, P. Meera, and J.L. Vergara. 2006. Quantitative evaluation of mammalian skeletal muscle as a heterologous protein expression system. *Protein Expr. Purif.* 47:281–288.

Dona, M., M. Sandri, K. Rossini, I. Dell'Aica, M. Podhorska-Okolow, and U. Carraro. 2003. Functional in vivo gene transfer into the myofibers of adult skeletal muscle. *Biochem. Biophys. Res. Commun.* 312:1132–1138.

Falk, G., and P. Fatt. 1964. Linear electrical properties of striated muscle fibers observed with intracellular microelectrodes. *Proceedings of the Royal Society of London Series B.* 160:69–123.

Fernandez, J.M., R.E. Taylor, and F. Bezanilla. 1983. Induced capacitance in the squid giant axon. Lipophilic ion displacement currents. *J. Gen. Physiol.* 82:331–346.

Gage, P.W., and R.S. Eisenberg. 1967. Action potentials without contraction in frog skeletal muscle fibers with disrupted transverse tubules. *Science.* 158:1702–1703.

Gerald, C.F. 1978. Applied Numerical Analysis. Second edition. Addison-Wesley Publishing Company, Reading, MA. 518 pp.

Gonzalez, J.E., and M.P. Maher. 2002. Cellular fluorescent indicators and voltage/ion probe reader (VIPR) tools for ion channel and receptor drug discovery. *Receptors Channels.* 8:283–295.

Gonzalez, J.E., and R.Y. Tsien. 1995. Voltage sensing by fluorescence resonance energy transfer in single cells. *Biophys. J.* 69:1272–1280.

Gonzalez, J.E., and R.Y. Tsien. 1997. Improved indicators of cell membrane potential that use fluorescence resonance energy transfer. *Chem. Biol.* 4:269–277.

Heim, R., and R.Y. Tsien. 1996. Engineering green fluorescent protein for improved brightness, longer wavelengths and fluorescence resonance energy transfer. *Curr. Biol.* 6:178–182.

Heiny, J.A., and J. Vergara. 1982. Optical signals from surface and T system membranes in skeletal muscle fibers. Experiments with the potentiometric dye NK2367. *J. Gen. Physiol.* 80:203–230.

Heiny, J.A., F.M. Ashcroft, and J. Vergara. 1983. T-system optical signals associated with inward rectification in skeletal muscle. *Nature.* 301:164–166.

Kim, A.M., and J.L. Vergara. 1998a. Fast voltage gating of Ca^{2+} release in frog skeletal muscle revealed by supercharging pulses. *J. Physiol.* 511(Pt 2):509–518.

Kim, A.M., and J.L. Vergara. 1998b. Supercharging accelerates T-tubule membrane potential changes in voltage clamped frog skeletal muscle fibers. *Biophys. J.* 75:2098–2116.

Loew, L.M. 1993. Potentiometric Membrane Dyes. *In* Fluorescent and Luminescent Probes for Biological Activity. W.T. Mason, editor. Academic Press, London. 50–160.

Magde, D., R. Wong, and P.G. Seybold. 2002. Fluorescence quantum yields and their relation to lifetimes of rhodamine 6G and fluorescein in nine solvents: improved absolute standards for quantum yields. *Photochem. Photobiol.* 75:327–334.

Moriyoshi, K., L.J. Richards, C. Akazawa, D.D. O'Leary, and S. Nakanishi. 1996. Labeling neural cells using adenoviral gene transfer of membrane-targeted GFP. *Neuron.* 16:255–260.

Oberhauser, A.F., and J.M. Fernandez. 1995. Hydrophobic ions amplify the capacitive currents used to measure exocytotic fusion. *Biophys. J.* 69:451–459.

Patterson, G.H., D.W. Piston, and B.G. Barisas. 2000. Forster distances between green fluorescent protein pairs. *Anal. Biochem.* 284:438–440.

Patterson, G., R.N. Day, and D. Piston. 2001. Fluorescent protein spectra. *J. Cell. Sci.* 114:837–838.

Prasher, D.C., V.K. Eckenrode, W.W. Ward, F.G. Prendergast, and M.J. Cormier. 1992. Primary structure of the *Aequorea victoria* green-fluorescent protein. *Gene.* 111:229–233.

Rizzo, M.A., G.H. Springer, B. Granada, and D.W. Piston. 2004. An improved cyan fluorescent protein variant useful for FRET. *Nat. Biotechnol.* 22:445–449.

Rohr, S., and B.M. Salzberg. 1994. Multiple site optical recording of transmembrane voltage (MSORTV) in patterned growth heart cell cultures: assessing electrical behavior, with microsecond resolution, on a cellular and subcellular scale. *Biophys. J.* 67:1301–1315.

Schneider, M.F., and W.K. Chandler. 1973. Voltage dependent charge movement of skeletal muscle: a possible step in excitation-contraction coupling. *Nature.* 242:244–246.

Selvin, P.R. 2002. Principles and biophysical applications of lanthanide-based probes. *Annu. Rev. Biophys. Biomol. Struct.* 31:275–302.

Shaklai, N., J. Yguerabide, and H.M. Ranney. 1977. Interaction of hemoglobin with red blood cell membranes as shown by a fluorescent chromophore. *Biochemistry.* 16:5585–5592.

Siegel, R.M., F.K. Chan, D.A. Zacharias, R. Swofford, K.L. Holmes, R.Y. Tsien, and M.J. Lenardo. 2000. Measurement of molecular interactions in living cells by fluorescence resonance energy transfer between variants of the green fluorescent protein. *Sci. STKE.* 2000:PL1.

Simon, B.J., and K.G. Beam. 1985a. The influence of transverse tubular delays on the kinetics of charge movement in mammalian skeletal muscle. *J. Gen. Physiol.* 85:21–42.

Simon, B.J., and K.G. Beam. 1985b. Slow charge movement in mammalian skeletal muscle. *J. Gen. Physiol.* 85:1–19.

Stryer, L., and R.P. Haugland. 1967. Energy transfer: a spectroscopic ruler. *Proc. Natl. Acad. Sci. USA.* 58:719–726.

Tsien, R.Y., B.J. Bacskai, and S.R. Adams. 1993. FRET for studying intracellular signalling. *Trends Cell Biol.* 3:242–245.

Umeda, Y., T. Marui, Y. Matsuno, K. Shirahashi, H. Iwata, H. Takagi, K. Matsumoto, T. Nakamura, A. Kosugi, Y. Mori, and H. Takemura. 2004. Skeletal muscle targeting in vivo electroporation-mediated HGF gene therapy of bleomycin-induced pulmonary fibrosis in mice. *Lab. Invest.* 84:836–844.

Williams, A.T.R., S.A. Winfield, and J.N. Millar. 1983. Relative fluorescence quantum yields using a computer-controlled luminescence spectrometer. *Analyst.* 108:1067–1071.

Woods, C.E., D. Novo, M. DiFranco, and J.L. Vergara. 2004. The action potential-evoked sarcoplasmic reticulum calcium release is impaired in mdx mouse muscle fibres. *J. Physiol.* 557:59–75.

Woods, C.E., D. Novo, M. DiFranco, J. Capote, and J.L. Vergara. 2005. Propagation in the transverse tubular system and voltage dependence of calcium release in normal and mdx mouse muscle fibres. *J. Physiol.* 568:867–880.

Zhang, F.L., and P.J. Casey. 1996. Protein prenylation: molecular mechanisms and functional consequences. *Annu. Rev. Biochem.* 65:241–269.